Revision 2

In-situ characterization of oxalic acid breakdown at elevated *P* and *T*: Implications for organic C-O-H fluid sources in petrologic experiments

Francis M. McCubbin[1,2], Dimitri A. Sverjensky[2,3], Andrew Steele[2], and Bjorn O. Mysen[2]

[1]Institute of Meteoritics, Department of Earth and Planetary Sciences, University of New Mexico, Albuquerque, New Mexico 87131-1126, U.S.A.

[2]Geophysical Laboratory, Carnegie Institution of Washington, 5251 Broad Branch Rd., N.W, Washington, DC 20015

[3]Department of Earth and Planetary Sciences, The Johns Hopkins University, Baltimore, MD 21218, USA

***** Author to whom correspondence should be addressed. Email: fmccubbi@unm.edu

Abstract

Decomposition of oxalic acid in the presence of water was examined in a hydrothermal diamond anvil cell up to 800°C and 970-1480 MPa as a function of oxygen fugacity to assess its usefulness as a C-O-H fluid source in petrologic experiments. Fluid, vapor, and solid species were identified *in-situ* at elevated temperature and pressure with Raman spectroscopy and optical microscopy. Under oxidizing conditions (buffered by the reaction $NiO \leftrightarrow Ni + \frac{1}{2}O_2$), oxalic acid decomposes to carbon dioxide and water. Under reducing conditions (buffered by the reaction $Mo + O_2 \leftrightarrow MoO_2$), oxalic acid decomposes to methane and hydrogen. Under unbuffered conditions, at intermediate oxygen fugacity (approximately 0 to 1 log units below the fayalite-quartz-magnetite buffer), oxalic acid disproportionates to graphite and minor methane and carbon dioxide. The results from the Ni-NiO-buffered and Mo-MoO_2-buffered experiments result in observed fluid species that are similar to those predicted by previous investigations. However, there are substantial differences between our results and previous studies of oxalic acid decomposition in the unbuffered experiment that was within a log unit of the fayalite-magnetite-quartz (FMQ) buffer. These include the detection of aqueous C-H species at temperatures as low as 400°C and a solid graphite-like phase at 800°C. These differences can be explained if we consider that aqueous H_2 in our experiment reacted to form the C-H species, instead of being lost via diffusion through the H_2-permeable capsules used in previous studies. Consequently, for experiments within about 1 log unit of the FMQ buffer curve, oxalic acid is likely a poor choice for a C-O-H fluid source because the formation of graphitic carbon would result in significant deviations from the expected C-O-H fluid composition and concentration (i.e., $CO_2 + H_2O$). At oxygen fugacities outside a log unit of FMQ, the observed fluid species are similar to those predicted by previous investigations and the use of oxalic acid as a C-O-H fluid source is permissible from the perspective of oxygen fugacity, although other system parameters (e.g. sample geometries, capsule thickness, capsule materials, gasket materials, wall thickness) must still be considered.

Keywords: Hydrothermal diamond-anvil cell, Raman spectroscopy, oxygen fugacity, magmatic volatiles, water, carbon

Introduction

Volatiles in the C-O-H system (O_2, H_2O, H_2, CO_2, CO, CH_4) dominate the volatile budget of the silicate Earth (Jambon, 1994) and are likely to play at least some role in geologic systems on the other terrestrial bodies. The solubility and solution mechanisms of C-O-H components in melts and fluids depends upon several system parameters, including bulk composition, temperature, pressure, and oxygen fugacity (i.e., Dixon et al., 1995; Eggler et al., 1979; Jakobsson and Holloway, 1986; Jakobsson and Oskarsson, 1990; Mysen et al., 1975; Saxena and Fei, 1987; Ulmer and Luth, 1991). Many experiments have been conducted to investigate the C-O-H system as a function of these parameters. However, most of the existing experiments were not analyzed *in-situ* at elevated pressure and temperature but were analyzed after the experimental samples had been returned to ambient conditions. Furthermore, many of the C-O-H experiments contain organic compounds (i.e., oxalic acid, hydrated oxalic acid, various oxalates, stearic acid, guanidine carbonate, tetrakis-silane) as a C-O-H fluid source. The presumed C-O-H fluid composition within those experiments relies heavily on assumptions that the organic compound will break down in a predictable manner and remain stoichiometric as the organic compound decomposes. Problems arise if the thermobarometric breakdown products of the selected organic compound include insoluble refractory organic compounds (IROC) that are stable or metastable at the elevated pressure and temperature conditions of the experiment. Some of these IROCs include graphite, macromolecular carbon, polycyclic aromatic hydrocarbons (PAH), and insoluble amorphous carbon (Eck et al., 1966; Steele et al., 2007; 2012a,b; Stein,

1978; 1991; Stein and Fahr, 1985). A few of these compounds are stable at temperatures greater than 2500°C (Stein, 1978; Stein and Fahr, 1985). If present as a thermal breakdown product of the organic compound used as a C-O-H fluid source, fluid compositions in the experiments would deviate from the expected C:O:H ratio.

Many of the previous experiments that included C-O-H components and used organic reagents as a C-O-H source have relied heavily on thermodynamic predictions that assumed equilibrium; however, kinetic effects, diffusive loss of volatile components, as well as back-reaction during cooling of an experiment are difficult to assess in the quenched run products (Brooker et al., 1998; Cesare, 1995; Holloway et al., 1968; Holloway and Reese, 1974; Morgan et al., 1992; Mysen and Yamashita, 2010). Consequently, *in-situ* analysis of the thermobarometric breakdown of a given organic compound should be determined before deciding on the appropriate compound to be used as a C-O-H fluid source in petrologic experiments. In particular, the decomposition of the organic compound should be assessed as a function of oxygen fugacity because the speciation within the C-O-H system is very sensitive to this parameter.

The hydrothermal diamond anvil cell (HDAC) is ideal for this assessment. It allows for experimental conditions up to 2500 MPa and 1200°C and can be coupled with *in-situ* spectroscopic analysis and microscopic observations (Bassett et al., 1993). In the present study, we used the HDAC to observe the breakdown of oxalic acid in aqueous solution to 800°C and 970-1480 MPa. The chemical species (in fluid, vapor, and solid) were determined *in-situ* throughout the experiments using Raman spectroscopy.

Oxalic acid was chosen for this study because it is one of the most commonly used organic C-O-H fluid sources in petrologic experiments at high pressure and temperature (i.e., Aranovich

and Newton, 1999; Cherniak and Watson, 2007; 2010; Draper and Green, 1997; Holloway et al., 1968; Holloway and Reese, 1974; Kesson and Holloway, 1974; Litvinovsky et al., 2000; Rosenbaum and Slagel, 1995). Thermal decomposition products of oxalic acid have been investigated previously, both experimentally and theoretically. At low temperatures (i.e., <150°C) the most common breakdown products include CO_2, HCOOH (formic acid), CO, and H_2O (Clark, 1955; Kakumoto et al., 1987; Lapidus et al., 1964; Nieminen et al., 1992; Noyes and Wobbe, 1926; Wobbe and Noyes, 1926; Yamamoto and Back, 1985). At higher temperatures analogous to hydrothermal, metamorphic, and igneous systems in planetary interiors, the breakdown products are reported to include CO_2, CO, H_2O, CH_4, H_2, graphite, and supercritical C-O-H fluids depending on experimental conditions (Holloway et al., 1968; Holloway and Reese, 1974; Kesson and Holloway, 1974; Morgan et al., 1992). The experimental results have been compared to results of thermodynamic calculations (using a database that includes standard state data for organic compounds) to assess whether or not equilibrium was attained during the experiments. In the present study, we compare our in-situ observations to previous investigations that assessed quenched run products only. We then use our data to assess the reliability of using oxalic acid as a C-O-H fluid source in petrologic experiments.

Experimental methods

Starting materials

Oxalic acid dihydrate [$C_2H_2O_4$•$2H_2O$] powder was mixed with double-distilled deionized H_2O to obtain a 160 millimolar (mM) solution of oxalic acid [$C_2H_2O_4$]. This concentration was chosen for three reasons. First, the concentration is high enough to detect C-O-H fluid species in solution, the exsolved vapor, and precipitated solid phases by Raman spectroscopy. Second, the oxalic acid concentration is low enough that the fluid pressure-volume-temperature (PVT)

properties do not deviate substantially from that of pure H_2O, making possible a pressure calibration of our HDAC using H_2O isochors (Bassett et al., 1996; Wagner and Pruss, 2002). Third, the concentration was well below the 1 bar, 25°C saturation limit of oxalic acid in H_2O (i.e., 14.3g/100mL or a 1.59 molar solution), so we were able to load the gaskets without forming unwanted crystal-liquid mixtures. Minor evaporation during sample loading would not drive the composition substantially towards oxalic acid saturation.

Hydrothermal diamond anvil cell (HDAC) experiments

An externally-heated hydrothermal diamond anvil cell (HDAC) (Bassett et al., 1993; Bassett et al., 1996) with 1 mm culets was used for all of the experiments. Analysis of the experiments was conducted *in-situ* at high temperature and pressure using Raman spectroscopy and optical microscopy. Temperatures were monitored and controlled to within ±1°C with chromel–alumel thermocouples in contact with the diamond surfaces of the upper and lower diamond anvils. The temperatures were calibrated against the melting temperature of NaCl (801°C at ambient pressure). Iridium gaskets with a 500μm central hole and 125μm thickness (these dimensions are determined prior to experiments) were used for sample containment. A gas mixture of 99% Ar and 1% H_2 was used to flow through the cell during each experiment to prevent oxidation of the metallic parts and decomposition of the diamond anvils during the high-temperature portions of the experiments.

Controlling oxygen fugacity in the HDAC. For experiments that were to be conducted under reducing conditions, the oxalic acid solution was loaded with a ~200 μm long, 70 μm diameter Mo^0 wire. During the experiment, both water and aqueous oxalic acid components would likely react with the molybdenum, but the dominant reaction in the system would be the following:

$$Mo^0 + 2H_2O \leftrightarrow MoO_2 + 2H_2 \quad [1]$$

This reaction would drive the oxygen fugacity (f_{O2}) of the experiment to reducing conditions that reach the Molybdenum-Molybdenum oxide buffer (MMO). This $\log f_{O2}$ value is approximately equal to that of the iron-wüstite buffer (IW) at the maximum P-T conditions for the HDAC experiments in the present study (Figure 1.; O'Neill and Pownceby, 1993; O'Neill, 1986). This technique for controlling f_{O2} in a HDAC was previously described by Mysen and Yamashita (2010). They reported that aqueous Mo-species do not become a major constituent in the fluid phase during the experiment (i.e., < 1 wt.% Mo). It is important to note that the MMO buffer is considered to be a lower limit estimate for the f_{O2} of our experiment because it is difficult to assess whether the reactive metal surface of the Mo^0 wire was completely coated with MoO_2, which would isolate the Mo^0 interior from the fluid and prevent reaction [1] from proceeding until an equilibrium f_{H2}/f_{H2O} was attained. This problem would be amplified by loss of H_2 from the system.

For experiments that were to be conducted under oxidizing conditions, the oxalic acid solution was loaded with NiO powder and Ni^0 powder. During the experiment, it was predicted that NiO would react with the aqueous oxalic acid components in the solution according to the reaction:

$$NiO + C_2H_2O_4 \leftrightarrow Ni^0 + H_2O + 2CO_2 \quad [2]$$

This reaction would buffer the oxygen fugacity (f_{O2}) to oxidizing conditions equal to the Nickel-Nickel oxide f_{O2} buffer (NiNiO) up to the point where all NiO would be consumed to make Ni metal (complete consumption of NiO during the experiment could occur due to H_2 permeation into the sample chamber from the Ar-H gas envelope around the diamond anvils). The NiNiO buffer is approximately 5 log units more oxidizing than the iron-wüstite buffer (IW) at the

maximum P-T conditions for the HDAC experiments in the present study (Figure 1.; Holmes et al., 1986; O'Neill and Pownceby, 1993).

One of the experiments was run unbuffered with respect to oxygen fugacity, but calculations using the program GFluid (Zhang and Duan, 2009; 2010), which calculates oxygen fugacity of a C-O-H fluid based on the fluid composition, indicate that the experiment ranged from an oxygen fugacity that was approximately equal to the FMQ oxygen fugacity buffer curve at low P-T conditions (i.e., 400°C and 730 MPa) and ranged as low as about 1 log unit below the FMQ buffer curve at the peak conditions of the experiment (i.e., 800°C and 1450 MPa). Therefore, although this experiment was not buffered with respect to oxygen fugacity, the range in oxygen fugacity for the entire duration of the experiment was within 1 log unit of the FMQ buffer curve. This f_{O2} value is approximately 3.5 log units above that of the IW buffer at the maximum P-T conditions for the HDAC experiments in the present study (Figure 1.; O'Neill, 1987; O'Neill and Pownceby, 1993).

Estimation of Pressure in the HDAC experiments. Pressure was computed using the equation-of-state (EoS) of pure H_2O (PVT data from Wagner and Pruss, 2002) in a constant-volume sample container (Bassett et al., 1996). To ensure gasket quality (defined as having constant gasket-volume behavior) during a high temperature/pressure experiment, the iridium gasket was run with pure double-distilled H_2O before loading it with the oxalic acid solution. This "pressure-conditioning" involved loading the gasket with double-distilled deionized water and increasing temperature, and hence pressure, to those of the maximum run conditions. This process was repeated until constant gasket-volume behavior was ascertained by gas bubble disappearance and reappearance (liquid-vapor homogenization) at the same temperature during heating and cooling of the HDAC containing only H_2O and air (see also Mysen, 2009 for details

of this procedure). This procedure did not work every time, as some gaskets changed volume with each episode of heating, so these gaskets were discarded. This procedure had a secondary advantage of being an effective method for removing carbon contamination from the gasket before loading the sample (Schmidt, 2009). The temperature difference between appearance and disappearance of bubbles was typically <10°C. Subsequent to pressure-conditioning, the oxalic acid + H_2O solution was loaded into the central hole of the iridium gasket. Importantly, the 160mM solution of oxalic acid is not pure water, so the pressure calculations will have a larger uncertainty than that described above for a pure H_2O system. Given the low concentration of oxalic acid in the aqueous solution (160mM), the pressures are going to be similar to those calculated using the PVT properties of pure H_2O. The P-T path for each experiment is dependent upon the liquid density, which we determined using the liquid-vapor homogenization temperature. To account for changes in fluid density from the breakdown of oxalic acid components during heating, the density of the solution for each experiment was determined based on the liquid-vapor homogenization temperature during heating and cooling to determine the pressure for each heating and cooling path, respectively. The maximum pressure was taken to be the midpoint between the pressure computed from the fluid density during heating and the pressure computed from the fluid density during cooling. The largest difference in liquid-vapor homogenization temperature during heating and cooling occurred in the Mo-wire-bearing experiment due to the breakdown of H_2O to H_2 and oxidation of Mo to MoO_2 that occurred in addition to the breakdown of oxalic acid components.

Analytical methods and thermodynamic modeling

Raman spectroscopy and optical microscopy

Experiments were monitored optically using reflected and transmitted visible light microscopy during each experiment. Density was determined for each of our oxalic-acid solutions by observing the temperature of liquid-vapor homogenization during heating and cooling, and those temperatures and densities are reported in Table 1. Two of the experiments (unbuffered and Ni-bearing) had vapor bubbles at 25°C that dissolved into solution during the tightening of the screws on the HDAC, so a homogenization temperature of 25°C was used for these experiments. The liquid-vapor homogenization temperatures during cooling were used to compute density and pressure during the cooling path for each experiment. The fluid density during cooling was typically lower than during heating (Table 1).

The speciation of the fluid during each of the experiments was probed with a Jasco model NRS-3100 confocal microRaman spectrometer. This spectrometer is equipped with a single monochromator and employs a holographic notch filter and holographic gratings with 600, 1200, or 2400 gratings/mm. A 50× magnification/0.42 N.A. objective lens was employed. A 532 nm laser operating at 7 mW was used for sample excitation. Signal detection was accomplished with an Andor Model DV401-F1 1024 × 128 pixel (25 μm pixel size) Peltier-cooled CCD. Acquisition time was typically 180 sec/CCD window and 2 acquisitions/window.

Raman spectroscopic measurements were conducted by first recording spectra of the sample at ambient conditions in the diamond anvil cell. The oxalic acid solution in the diamond cell was then raised to 800°C and 970-1480 MPa, and optical and spectroscopic observations were conducted at 100°C intervals both as the experiments were heated and cooled. The heating/cooling rate between intervals was approximately 1°C/s. With this procedure, the samples remained at each temperature between 20 and 30 minutes during optical and Raman

spectroscopic analysis. Background subtraction and curve-fitting of Raman spectra were carried out using the commercial software package ACD LABS Spec manager V12.

Thermodynamic modeling

Aqueous speciation and chemical mass transfer calculations (Helgeson, 1979) were used to model the aqueous fluid phase chemistry in the oxalic acid decomposition experiments. Calculations were carried out using the computer codes EQ3NR/EQ6 (Wolery, 1983; 1984) modified to model supercritical aqueous solution chemistry. The thermodynamic data used are from an internally consistent compilation from the following sources: minerals (Helgeson et al., 1978), metallic Mo and MoO_2 (Robie et al., 1978), and aqueous species (Shock, 1995; Shock and Helgeson, 1988; 1990; Shock et al., 1989; Shock et al., 1997; Sverjensky et al., 1997). Equilibrium constants were calculated with SUPCRT92 (Johnson et al., 1992) and incorporated into the database for EQ3NR/EQ6. Calculations were limited to a maximum pressure of 500 MPa corresponding to the upper limit for available thermodynamic properties of the aqueous species. At this pressure, the experimental temperature in the HDAC is approximately 330-450°C. Therefore, the results presented from this modeling correspond to the equilibrium conditions at 450°C and 500 MPa (see Table 1 for P-T relationship in the experiments).

An initial aqueous speciation calculation of dilute oxalic acid in water was carried out at 25°C and 500 MPa. The aqueous solution also included trace amounts of Mo. The output from this speciation calculation was used as input to a reaction path calculation (using EQ6) at 450°C and 500 MPa. The 160 mM aqueous solution was reacted with 160 millimoles per kg water of oxalic acid with and without excess metallic Mo as an additional reactant. These calculations provide a Gibbs free energy minimization of the bulk composition of the three systems of

interest: oxalic acid + water + Mo^0 wire, oxalic acid + water + NiO powder + Ni^0 powder, and oxalic acid + water.

Results

A summary of experimental conditions and phases present at each heating and cooling step is shown in Table 1. The densities for each of the experimental liquids were determined based on the liquid-vapor homogenization temperature during heating and cooling. During the heating path the liquid-vapor homogenization temperatures were 25°C for the unbuffered and Ni^0+NiO experiments and 162°C for the Mo-bearing experiment (corresponding to fluid densities of 0.997 and 0.905 g /cm^3, respectively). Upon cooling, the liquid-vapor homogenization temperatures were 90°C for the unbuffered experiment, 50°C for the Ni^0+NiO experiment, and 225°C for the Mo-bearing experiment (corresponding to fluid densities of 0.965, 0.988, and 0.834 g /cm^3, respectively). Although the temperature/pressure paths of the three experiments were similar, the Ni^0+NiO, and unbuffered experiments reached a higher pressure (1480 and 1450 MPa, respectively) than the Mo^0 experiment (970 MPa) (Table 1).

Procedural blank experiment

We performed a procedural blank experiment mirroring our run conditions for the oxalic acid experiments; but in our blank experiment, we added only pure double-distilled deionized H_2O into the central hole of an Ir gasket. The results of this experiment did not yield any detectable C-H species in the resulting fluid over the entire run duration, which was also reported by Mysen, 2010, which used run conditions similar to those employed here. Although Chou and Anderson (2009) reported that pure H_2O in a hydrothermal diamond anvil cell experiment could react with the diamond anvil and metallic gasket (including Re, Ir, and Inconel) to form various C-bearing species including methane (CH_4) and carbon dioxide (CO_2), we do not consider the

diamond anvils to have been a significant source of carbon contamination in our HDAC experiments. Our results are consistent with another recent study that used a Bassett-style HDAC to observe pure water at elevated pressures and temperatures (Kawamoto et al., 2004), and carbon-species were not detected in the fluids of those experiments, although those experiments were at lower temperature.

160 mM oxalic acid experiment with Mo^0 wire

Optical microscopy. Transmitted and reflected light photomicrographs of the experimental charge before heating are shown in Figure 2a. Upon heating the vapor bubbles present at the time of loading disappeared at 162°C. From the point of vapor loss, there was no apparent change to the Mo^0-bearing system visually until the heating step from 400-500°C. At 400-500°C, the Mo^0 wire began to oxidize, forming small needles of MoO_2 (confirmed by Raman spectroscopy in Figure 3; Dieterle and Mestl, 2002), similar to those reported by Mysen and Yamashita (2010) (Figure 2b). Once formed, the MoO_2 phase persisted throughout the duration of the experiment; however, the reaction did not go to completion, as there was still Mo^0 left at the end of the experiment. However, as noted above, it was difficult to assess whether the reactive metal surface of the Mo^0 wire reached complete oxidation, leaving a metal interior that no longer communicated with the aqueous fluid; therefore, the MMO buffer should be considered a lower limit on the oxygen fugacity of the system. During cooling, a vapor phase exsolved from the fluid (Figure 2c) at 225°C. The vapor volume increased as the experiment cooled to 100°C.

Raman spectroscopy. During heating of the Mo^0-bearing sample, there was no apparent change in fluid-speciation until 500°C. At this temperature, a broad peak centered at 2905 cm^{-1}

297 appears (Figure 4a, b). This peak is assigned to C-H stretch vibrations in aqueous C-H_n species.
298 Its appearance likely marks the initial breakdown of the aqueous oxalic acid.

299 The wavenumber of the 2905 cm^{-1} peak increased to 2920 cm^{-1} at 600°C and remained at
300 this position until 800°C where it shifted to lower wavenumber (2910 cm^{-1}). As the temperature
301 and pressure of the experiment was lowered, the spectral position of this peak decreased from
302 2910 cm^{-1} to 2900 cm^{-1}, and its intensity increased until 300°C (Table 2). During the cooling step
303 from 300°C to 200°C, vapor bubbles exsolved from the fluid, and the intensity of the 2900 cm^{-1}
304 peak in the fluid decreased considerably. Subsequent cooling steps resulted in a decreased
305 intensity of the 2900 cm^{-1} peak concomitant with the increased volume of the vapor bubbles.

306 Subsequent to the cooling step from 800°C to 700°C, a peak centered at 4133 cm^{-1}
307 appeared (Figure 4a, c). This peak is assigned to the H-H molecular vibrations of H_2 (Bezmen et
308 al., 1991; Morgan et al., 1992; Socrates, 2001). As the fluid was cooled, its wavenumber varied
309 between 4126 cm^{-1} and 4133 cm^{-1}. Its intensity increased until 300°C and dropped subsequent to
310 vapor-phase exsolution from the fluid (Figure 4a, c), similar to the intensity behavior of the 2900
311 cm^{-1} peak (Figure 4a, b). The Raman spectra of these bubbles contain several very sharp peaks at
312 356 cm^{-1}, 589 cm^{-1}, 815 cm^{-1}, 1034 cm^{-1}, 2900 cm^{-1}, 3009 cm^{-1}, 3064 cm^{-1}, 3576 cm^{-1}, 3904 cm^{-1},
313 4117 cm^{-1}, and 4146 cm^{-1} (Figure 5). The peaks at 356 cm^{-1}, 589 cm^{-1}, 815 cm^{-1}, 1034 cm^{-1}, 4117
314 cm^{-1}, and 4146 cm^{-1} are assigned to H_2 (Bezmen et al., 1991; Morgan et al., 1992; Socrates,
315 2001). The peaks at 2900 cm^{-1}, 3009 cm^{-1}, 3064 cm^{-1} are associated with CH_4 (Lin-Vien et al.,
316 1991; Socrates, 2001, Lu et al., 2007). There are peaks at 3576 cm^{-1} and 3904 cm^{-1} that appear in
317 the spectrum of the vapor phase and not in the fluid phase. Although the 3576 cm^{-1} peak is in the
318 same region as H_2O (Frantz et al., 1993; Kawamoto et al., 2004; McMillan and Remmele, 1986;
319 Van Thiel et al., 1957; Velde, 1983), specifically hydrogen-bonded OH stretching modes (Lin-

Vien et al., 1991), it may not be from H_2O vapor due to its correlation in intensity with the peak at 3904 cm^{-1}, which is outside of the range for OH modes. We were unable to identify the molecular species responsible for these peaks, but we can confirm that they are not due to Raman vibration modes from any known organic molecular group (Lin-Vien et al., 1991; Socrates, 2001), and we suspect that they could be the result of photoluminescence from a minor species within the vapor.

Thermodynamic Calculations. Reaction of 160 millimoles oxalic acid with 1.0 kg water and 20 moles of Mo at 450°C and 500 MPa resulted in the aqueous fluid speciation presented in Table 3. The reactions resulted in the conversion of 13 moles of Mo to MoO_2 at which point the fluid reached equilibrium with respect to both the metal and the oxide. Other than CH_4, aqueous C-bearing species were predicted to be present in only trace amounts. The computed $\log f_{O2}$ of the system was equal to approximately -32, which is displaced by -6.5 log units below the QFM oxygen buffer at 450°C and 500 MPa (approximately equal to IW -1). It should be noted that the aqueous species concentrations (e.g. the 592 mM CH_4) reflect consumption of 26 moles of water during the conversion of the 13 moles of Mo metal to its oxide. During this reaction, 25 moles of aqueous H_2 were produced. This is far in excess of what could be dissolved in the aqueous fluid. In the model, only aqueous solutions and solids are explicitly treated. There is no provision for an additional coexisting low density gas-like phase. However, the production of so much H_2 from the oxidation of the Mo metal suggests that a separate H_2-rich gas-like phase should form. This phase was not observed in the experiments until low temperature, which may indicate either the extent of reaction of Mo with water did not reach equilibrium, some of the H_2 escaped from the system by leakage, or a combination of both processes.

Other important features of the model are that the fluid is computed to be extremely undersaturated with respect to graphite (about -24 kcal/mol). In addition, the concentration of aqueous Mo-species were predicted to be on the order of 4.34 x 10^{-11} molal, consistent with the conclusions of Mysen and Yamashita (2010) that $Mo_{(aq)}$ concentrations resulting from fluid interaction with Mo^0 wire in the HDAC (at the P-T conditions relevant to the present study) are below the detection limit of aqueous Mo-species by Raman spectroscopy.

160 mM oxalic acid experiment with NiO and Ni^0 powder

Optical microscopy. After initially loading the oxalic acid solution and Ni^0+NiO powder, there was a vapor bubble in the solution that dissolved as the screws on the HDAC were tightened. Transmitted and reflected light photomicrographs of the experimental charge after tightening of the screws and before heating are shown in Figure 6a. The NiO powder appeared to react with the solution immediately upon loading into the gasket. The powder noticeably increased in volume during the heating step from 100°C to 200°C (Fig. 6b), translucent crystals started to grow, including a single large crystal (Figure 6c). Above 300°C, the crystal began to react and reduce in volume, forming small metallic clusters of Ni^0 (Figure 6c); however, the reaction did not seem to go to completion because there appeared to be two phases left at the end of the experiment. During cooling, a vapor phase exsolved from the fluid (Figure 6d) at approximately 50°C, and the volume of the vapor increased with decreasing temperature.

Raman spectroscopy of the solid. Initial Raman analyses of the NiO powder before heating yielded a spectrum that was similar to α-$Ni(OH)_2$ or highly disordered β-$Ni(OH)_2$ (Figure 3b; Deabate et al., 2000; Desilvestro et al., 1986), which likely occurred by interaction of NiO with the hydrous component of the oxalic acid solution via the reaction:

$$NiO + H_2O \leftrightarrow Ni(OH)_2 \quad [3],$$

The $Ni(OH)_2$ powder noticeably increased in volume during the heating step from 100°C to 200°C (Fig. 6b), which corresponded to the formation of translucent crystals by optical microscopy. The Raman spectra of the translucent crystals was similar to the mineral zaratite [$Ni_3(CO_3)(OH)_4 \bullet 4(H_2O)$] (Figure 3; Frost et al., 2008), indicating the conversion of $Ni(OH)_2$ to a hydrated Ni carbonate. By 300^0C, $Ni(OH)_2$ was no longer detected in the experiment. The zaratite likely formed by reaction with the oxalic acid component of the fluid based on the following reaction:

$$7Ni(OH)_2 + C_2H_2O_4 + 4H_2O \leftrightarrow 2Ni_3(CO_3)(OH)_4 \bullet 4(H_2O) + Ni^0 \quad [4].$$

Above 300°C, the hydrated Ni carbonate began to react and reduce in volume, forming small metallic clusters of Ni^0 (Figure 6c); however, the reaction did not go to completion, as there was still hydrated Ni carbonate left at the end of the experiment (Figure 3). The activity of NiO may have deviated from unity because all of the NiO reacted to form $Ni(OH)_2$, followed by hydrated Ni carbonate, so the NiNiO oxygen buffer should be considered an upper limit on the oxygen fugacity of the system. Importantly, a Ni^{2+}-phase was present throughout the duration of the run, so we were likely within a log unit of NiNiO.

Raman spectroscopy of the fluid. During heating of the NiO+Ni^0-bearing sample, there was no apparent change in fluid-speciation during the entire sequence of heating to 800°C and cooling to 25°C. A vapor phase exsolved during cooling at 50°C, and the Raman spectra of these bubbles contain two small peaks on either side of the main diamond peak at 1389 cm^{-1} and 1286 cm^{-1} (Figure 7), both of which are indicative of CO_2 (Socrates, 2001; Yamamoto and Kagi, 2008). A high spectral resolution Raman analysis with the spectrometer centered at 2900 cm^{-1} was also conducted on the vapor bubbles, but no other peaks in this region were detected (Figure 7), indicating that C-H components were not detected in the vapor phase.

Thermodynamic Calculations.

Other than CO_2, aqueous C-bearing species were predicted to be present in only trace amounts (Table 3). The computed $\log f_{O2}$ of the system was equal to approximately -24.7, which is displaced by 1 log units above the QFM oxygen buffer at 450°C and 500 MPa. The fluid is computed to be undersaturated with respect to graphite (about -7 kcal/mol).

Unbuffered 160 mM oxalic acid experiment

Optical microscopy. Transmitted and reflected light photomicrographs of the experimental charge before heating are provided in Figure 2d. As the unbuffered experiment was heated, there was no apparent visual change until the heating step from 700-800°C. At 700-800°C, a dark phase began to precipitate on the diamond anvils (Figure 2e). After its formation, the phase persisted throughout the duration of the experiment. A vapor phase exsolved from the fluid upon cooling at approximately 90°C (Figure 2f), and the volume of the vapor increased with decreasing temperature.

Raman spectroscopy. As the unbuffered sample was heated, there was no apparent change in fluid-speciation until 400°C. At this temperature, a broad peak centered at 2907 cm^{-1} was detected (Figure 8a, c). This peak position is typically associated with aqueous C-H_n species (Chou et al., 1990; Dubessy et al., 1999; Socrates, 2001), which may mark the initial breakdown of the aqueous oxalic acid. The peak centered at 2907 cm^{-1} increased in intensity and wavenumber (2907-2935 cm^{-1}) as a function of increasing temperature and pressure, until the heating step from 700-800°C (Table 4). When heating from 700°C to 800°C, a thin layer of dark material precipitated on the diamond anvil surfaces and the broad peak centered at 2907-2923 cm^{-1} was not detected; although the peak reappeared during the cooling step from 700°C to 600°C (Figure 8a, c). The broad peak centered at 2907-2923 cm^{-1} disappeared once more during

411 the cooling step from 400°C to 300°C, and it was not detected in the fluid phase for the
412 remainder of the experiment. The Raman spectrum collected at 800°C included the appearance
413 of a broad peak centered at 1578 cm^{-1}, and this peak is likely associated with the thin layer of
414 dark material that precipitated between 700°C and 800°C (Figure 8a, b). The identity of the 1578
415 cm^{-1} peak is consistent with C=C bonds typically associated with graphite (Socrates, 2001; Steele
416 et al., 2007; 2010), however it is difficult to assess the degree of crystallinity of this phase
417 because the peak in graphite that indicates the degree of disorder (i.e., the D band at 1350 cm^{-1})
418 is masked by the large diamond peak. The height of the peak centered at 1578 cm^{-1} continued to
419 increase as temperatures cooled back to room temperature (Table 4). The peak center of the 1578
420 cm^{-1} peak remained relatively constant (perhaps with a slight increase in peak center position as
421 a function of decreasing temperature and pressure) during cooling, with the center position in the
422 1575 cm^{-1} to 1585 cm^{-1} range (Figure 8a, b and Table 4). A vapor phase exsolved from the fluid
423 below 100˚C (Figure 2f), and the Raman spectra of the vapor bubbles showed peaks at 1287 cm^{-1}
424, 1390 cm^{-1}, 2900 cm^{-1}, 3500 cm^{-1}, and 3850 cm^{-1} (Figure 9). Those at 1287 cm^{-1} and 1390 cm^{-1}
425 are assigned to CO_2 (Azbej et al., 2007; Chou and Anderson, 2009; Morgan et al., 1992; Rosso
426 and Bodnar, 1995). The peak at 2900 cm^{-1} is associated with CH_4 (Chou et al., 1990; Dubessy et
427 al., 1999; Socrates, 2001). There is a peak centered at approximately 3500 cm^{-1} that stands above
428 the broad peak resulting from H_2O that is observed in the fluid spectra. The 3500 cm^{-1} peak may
429 not be associated with H_2O in the vapor phase. Much like in the Mo-bearing experiment, the
430 peak coexists with another higher wavenumber peak (at 3850 cm^{-1}) that is inconsistent with OH
431 stretching modes. We have not identified the source for these peaks, but we suspect that they
432 could be the result of photoluminescence from a minor species within the vapor. Importantly, the

433 peaks do not seem to be Raman vibrational modes of any known organic molecular groups (Lin-
434 Vien et al., 1991; Socrates, 2001).

435 **Thermodynamic calculations**. In the absence of a solid reactant, reaction of 160
436 millimoles oxalic acid with 1.0 kg water at 450°C and 500 MPa resulted in the aqueous fluid
437 speciation presented in Table 3. The $\log fO_2$ of the system was predicted to be equal to
438 approximately -25.5, which is equal to that of the FMQ oxygen buffer at 450°C and 500 MPa
439 (O'Neill, 1987). Furthermore, this is consistent with calculations made in the program GFluid
440 (Zhang and Duan, 2009; 2010). It should be noted that the sum of the CO_2 and CH_4
441 concentrations comes to 321 millimolal (mM), rather than the 322 mM expected from the initial
442 oxalic acid concentration. This is a result of the fact that the aqueous species concentrations
443 include the additional water created by the decomposition of the initial oxalic acid into carbon
444 dioxide, methane, and water. The computed state of saturation of the fluid with respect to
445 graphite is about -4 kcal/mol (i.e. the fluid is undersaturated with respect to graphite at 450°C
446 and 500 MPa).

447 **Discussion**

448 The breakdown products of oxalic acid have been previously investigated under elevated
449 pressure and temperature conditions, and they are expected to follow from the reaction:

450 $$C_2H_2O_4 \leftarrow\rightarrow H_2O + CO_2 + CO \quad [5]$$

451 (Holloway et al., 1968; Morgan et al., 1992). The CO component of this reaction would undergo
452 the water-gas reaction:

453 $$CO + H_2O \leftarrow\rightarrow CO_2 + H_2 \quad [6]$$

454 with H_2 presumably being rapidly lost from the system via diffusion (Holloway et al., 1968;
455 Morgan et al., 1992). In the experimental apparatus' used by those workers, loss of H_2 is a

456 reasonable assumption since the samples were enclosed in H_2-permeable capsules. However, the
457 run-products were not analyzed *in-situ*, so only the final state of the system was observed.

458 The results of our experiment conducted under oxidizing conditions were also consistent
459 with previous investigations of the breakdown of oxalic acid at elevated oxygen fugacity that
460 demonstrate C-O-H fluids are dominated by H_2O and CO_2 species (Holloway et al., 1968;
461 Holloway and Jakobsson, 1986). The observed fluid species during the cooling part of the
462 experiments are consistent with the thermodynamic computations carried out during the present
463 study at 450°C and 500 MPa, which reflect equilibrium between Ni^0 and NiO. This lends support
464 to the notion that transformation of NiO to $Ni(OH)_2$ and then to $Ni_3(CO_3)(OH)_4 \bullet 4(H_2O)$ did not
465 dramatically affect the *a*NiO.

466 **Comparison with previous results under reducing conditions**

467 The results of our experiment conducted under reducing conditions are consistent with
468 observations made in previous experiments that assessed oxalic acid breakdown at low oxygen
469 fugacity. The C-O-H fluids were dominated by H_2O, CH_4, and H_2 species (Jakobsson and
470 Holloway, 1986; Jakobsson and Oskarsson, 1990; Kadik et al., 2004). From our in-situ analysis,
471 we were able to show that C-H speciation, as indicated by the broad Raman shift at ~2900 cm^{-1},
472 was observed at temperatures as low as 500°C. Importantly, this experiment provides evidence
473 that H-permeation from our experiments was incomplete on the time scale of the experiment.
474 This contrasts with previous experimental studies involving oxalic acid decomposition where
475 diffusive hydrogen loss was assumed and seemingly confirmed with the use of H_2-permeable
476 capsule materials (c.f., Holloway et al., 1968; Morgan et al., 1992).

477 **Divergence between *in-situ* analysis and previous experiments**

Our unbuffered experiment, which can be approximated to be at an oxygen fugacity near that of the QFM buffer at 450°C and 500 MPa, did not follow the expected reaction pathway for the breakdown of oxalic acid in the presence of H_2O (i.e., via reactions [5] and [6] Holloway et al., 1968; Morgan et al., 1992). By 400°C, the oxalic acid had disproportionated into C-H species and presumably C-O species that were not detected in the fluid. Considering reactions [5] and [6], the observed C-H_n Raman modes in the fluid spectra from 400-700°C can likely be explained if the H_2 species from reaction [6] reacted with C-species instead of escaping from the system. In support of this, aqueous methane was predicted by the thermodynamic model of the unbuffered experiment at 450 °C and 500 MPa (Table 3). Therefore, reactions that involve the formation of CH_4 are likely possible in this system, in addition to reactions [5] and [6] reported previously, including reactions such as:

$$2H_2 + 2CO \leftarrow \rightarrow CH_4 + CO_2 \quad [7]$$

and

$$4H_2 + CO_2 \leftarrow \rightarrow CH_4 + 2H_2O \quad [8].$$

At 800°C, our system showed an additional difference from the previous experimental studies (Holloway et al., 1968; Morgan et al., 1992) with the precipitation of a graphitic carbon phase. The appearance of this phase nearly coincided with the crossing of the f_{O2} of the unbuffered experiment and the GCO f_{O2} buffer curve along the P-T path of the experiment, which is within about a log unit of the FMQ and GCO buffer-curve intersection (Figure 1). Although this coincidence in oxygen fugacity should not induce the precipitation of graphite, at f_{O2} near the FMQ buffer, the solubility of C in aqueous fluids is quite low as it coincides with a coupled minimum in oxygen fugacity and in hydrogen fugacity (see Sharp et al., 2013). The lower solubility of C at this oxygen fugacity is consistent with thermodynamic calculations

indicating the unbuffered experiment was much closer to the graphite saturation surface at 450°C and 500 MPa than the two buffered experiments.

The graphitic carbon phase persisted for the remainder of the experimental sequence (decreasing temperature), causing the fluid composition to deviate significantly from that predicted by Holloway (1968) for oxalic acid breakdown under oxygen fugacities near FMQ. This C-phase was not predicted by our thermodynamic calculations at 450°C and 500 MPa where the fluid was predicted to have been slightly undersaturated with respect to graphite (Table 3). However, based on previous studies on graphite stability (i.e., Connolly, 1995; Luque et al., 1998; Ulmer and Luth, 1991), graphite was likely stable close to the peak conditions of our experiment (800 °C and 1450 MPa).

Oxalic acid as a C-O-H fluid source in experimental petrology

The use of inorganic compounds such as silver oxalate ($Ag_2C_2O_4$) and aluminum carbide (Al_4C_3) are popular for adding volatile components to petrologic experiments (Behrens et al., 2009; Costa et al., 2003; Dixon et al., 1995; Lin and Bodnar, 2010); however, these methods can result in adding unwanted elements and components into experiments. Ideally, one would choose a C-O-H fluid composition and mix stoichiometric combinations of reliable organic compounds that would yield the desired C-O-H composition. Before this will be possible, the thermobarometric breakdown of various organic compounds needs to be tested, and this was the primary motivation for the present study. Although the experiments carried out in the present study are fairly simple compared to multi-component silicate systems, the results illustrate the importance of understanding organic compound decomposition at elevated pressure and temperature as a function of oxygen fugacity before use as a C-O-H fluid source in petrologic

523 experiments. We propose that any organic compound that is to be used as a C-O-H fluid source
524 in a petrologic experiment first be evaluated by the methods employed in the present study.

525 The breakdown products of oxalic acid produced under reducing conditions in our
526 experiment matches the molecular speciation reported from previous experimental studies and
527 calculations (i.e., H_2, CH_4, and H_2O). Although some H_2 permeation out of our system likely
528 occurred in our Mo-bearing HDAC experiment, no unexpected fluid species or solid phases
529 formed. Indeed, thermodynamic calculations suggest that the fluid was highly undersaturated
530 with respect to graphite at least at 450°C and 500 MPa. Therefore, the use of oxalic acid as a C-
531 O-H fluid source in reduced magmatic and hydrothermal systems is advisable from the
532 perspective of oxygen fugacity.

533 The resulting phases from the breakdown of oxalic acid observed in this study under
534 oxidizing conditions also match the molecular speciation reported from previous oxalic acid
535 breakdown studies and calculations (i.e., CO_2, and H_2O). No unexpected fluid species or solid
536 phases formed. Thermodynamic calculations suggest that the fluid was highly undersaturated
537 with respect to graphite at least at 450°C and 500 MPa. Therefore, from the perspective of
538 oxygen fugacity, the use of oxalic acid as a C-O-H fluid source in oxidized magmatic and
539 hydrothermal systems is advisable (i.e., >1 log unit above FMQ).

540 Our unbuffered oxalic acid breakdown experiment, estimated at an fO_2 within a log unit
541 of the FMQ buffer, deviated significantly from the simple water-gas reactions predicted for this
542 system (Holloway et al., 1968; Morgan et al., 1992). In particular, the formation of a graphite-
543 like phase and the formation of aqueous C-H species (possibly CH_4), with CO_2 provide a contrast
544 to previous studies. The unbuffered experiment illustrates potential problems with assumptions
545 about rapid H_2-diffusion in order to predict molar fluid ratios (e.g., Cherniak and Watson, 2007;

Cherniak and Watson, 2010; Draper and Green, 1997; Holloway et al., 1968; Litvinovsky et al., 2000; Morgan et al., 1992). We recommend that oxalic acid be avoided as a C-O-H fluid source in experiments conducted within about 1 log unit of the FMQ buffer. We do not wish to imply that all the experiments that have contained oxalic acid as a C-O-H fluid source deviated from their predicted C-O-H fluid composition because they likely experienced a different P-T path. However, the results presented here illustrate that run products should be inspected for the presence of graphitic carbon even if experiments are carried out in capsules reported to be permeable to H_2. Furthermore, it is good to consider the P-T path of the entire experiment with respect to the stability of the reagents used, especially organic compounds and hydrated phases. Although we discuss the potential use of oxalic-acid in petrologic experiments based on the breakdown behavior as a function of oxygen fugacity, we also note that other experimental parameters (e.g. sample geometries, capsule thickness, capsule materials, gasket materials, wall thickness) must also be considered when picking an appropriate reagent for a C-O-H fluid source.

Implications

Oxygen fugacity of magmatic systems in our own Solar System ranges from as low as about 7 units below the IW buffer on Mercury to approximately the magnetite-hematite (MH) buffer in some terrestrial lavas and at the surface of Venus (Fegley et al., 1997; McCubbin et al., 2012; Peng et al., 1997; Zhang et al., 2013; Zolotov et al., 2013). Furthermore, C is a ubiquitous element among the terrestrial planets and understanding carbon chemistry in the terrestrial planets is important for a wide range of processes from magmatism to astrobiology. Consequently the stability and fate of C-bearing species has relevance to natural geologic systems over a wide range of conditions. Experimental work on these systems that are aimed at

569 understanding C-species requires choosing an appropriate reagent that will yield an expected C-
570 O-H ratio under specific P-T-f_{O2} conditions without compromising composition (X). In the
571 present study, we have determined a method for assessing the appropriateness of such reagents
572 and have specifically shown that the use of oxalic acid is permitted as a C reagent in petrologic
573 experiments of planetary systems under a wide range of relevant oxygen fugacities.

574 **Acknowledgments**

575 This work benefitted greatly from discussions with Penelope L. King and Laura K. Burkemper.
576 We would also like to thank Malcolm J. Rutherford and Christian Schmidt for very helpful
577 comments that substantially improved the quality of the manuscript. We also acknowledge Keith
578 Putirka for his efforts as Associate Editor and Editor. FMM acknowledges fellowship support
579 from the Carnegie Institution of Washington, Geophysical Laboratory and support from NASA's
580 Cosmochemistry program (NNX11AG76G awarded to FMM). Portions of this research were
581 supported by NSF grant EAR-073418 to BOM. Support for DAS was provided by a NSF-NASA
582 Collaborative Research Grant to the Johns Hopkins University and the Carnegie Institution for
583 Science, the NASA Astrobiology Institute and DOE Grant DE-FG02-96ER-14616. AS
584 acknowledges support from NASA's Astrobiology Science and Technology for Exploring
585 Planets program and NASA's Mars Fundamental Research Program.

586 References cited

587

588 Andersen, D.J., Lindsley, D.H., and Davidson, P.M. (1993) QUILF - a Pascal program to assess
589 equilibria among Fe-Mg-Mn-Ti oxides, pyroxenes, olivine, and quartz. Computers &
590 Geosciences, 19, 1333-1350.

Aranovich, L.Y., and Newton, R.C. (1999) Experimental determination of CO_2-H_2O activity-composition relations at 600-1000°C and 6-14 kbar by reversed decarbonation and dehydration reactions. American Mineralogist, 84, 1319-1332.

Azbej, T., Severs, M.J., Rusk, B.G., and Bodnar, R.J. (2007) *In situ* quantitative analysis of individual H_2O-CO_2 fluid inclusions by laser Raman spectroscopy. Chemical Geology, 237, 255-263.

Bassett, W.A., Shen, A.H., Bucknum, M., and Chou, I.M. (1993) A new diamond anvil cell for hydrothermal studies to 2.5 GPa and from 190 °C to 1200 °C. Review of Scientific Instruments, 64, 2340-2345.

Bassett, W.A., Tzy-Chung, W., Chou, I.M., Haselton, H.T., Frantz, J., Mysen, B.O., Huang, W.L., Sharma, S.K., and Schiferl, D. (1996) The hydrothermal diamond anvil cell (HDAC) and its applications. In M.D. Dyar, C. McCammon, and M.W. Schaefer, Mineral Spectroscopy: A tribute to Roger C. Burns, 5, p. 261-272. The Geochemical Society, Houston, TX.

Behrens, H., Misiti, V., Freda, C., Vetere, F., Botcharnikov, R.E., and Scarlato, P. (2009) Solubility of H_2O and CO_2 in ultrapotassic melts at 1200 and 1250 °C and pressure from 50 to 500 MPa. American Mineralogist, 94, 105-120.

Bezmen, N.I., Zharikov, V.A., Epelbaum, M.B., Zavelsky, V.O., Dikov, Y.P., Suk, N.I., and Koshemchuk, S.K. (1991) The system $NaAlSi_3O_8$ - H_2O - H_2 (1200°C, 2 kbar): The solubility and interaction mechanism of fluid species within melt. Contributions to Mineralogy and Petrology, 109, 89-97.

612 Brooker, R., Holloway, J.R., and Hervig, R. (1998) Reduction in piston-cylinder experiments:
613 The detection of carbon infiltration into platinum capsules. American Mineralogist, 83,
614 985-994.
615 Cesare, B. (1995) Graphite precipitation in C-O-H fluid inclusions: Closed-system compositional
616 and density changes, and thermobarometric implications. Contributions to Mineralogy
617 and Petrology, 122, 25-33.
618 Cherniak, D.J., and Watson, E.B. (2007) Ti diffusion in zircon. Chemical Geology, 242, 473-
619 483.
620 -. (2010) Li diffusion in zircon. Contributions to Mineralogy and Petrology, 160, 383-390.
621 Chou, I.M., and Anderson, A.J. (2009) Diamond dissolution and the production of methane and
622 other carbon-bearing species in hydrothermal diamond-anvil cells. Geochimica et
623 Cosmochimica Acta, 73, 6360-6366.
624 Chou, I.M., Pasteris, J.D., and Seitz, J.C. (1990) High-density volatiles in the system C-O-H-N
625 for the calibration of the laser Raman microprobe. Geochimica et Cosmochimica Acta,
626 54, 535-543.
627 Clark, L.W. (1955) The effect of water and of glycerol on the decarboxylation of oxalic acid.
628 Journal of the American Chemical Society, 77, 6191-6192.
629 Connolly, J.A.D. (1995) Phase diagram methods for graphitic rocks and application to the
630 system C-O-H-FeO-TiO_2-SiO_2. Contributions to Mineralogy and Petrology, 119, 94-116.
631 Costa, F., Scaillet, B., and Pichavant, M. (2004) Petrological and experimental constraints on the
632 pre-eruption conditions of Holocene dacite from Volcan San Pedro (36^o S, Chilean
633 Andes) and the importance of sulphur in silicic subduction-related magmas. Journal of
634 Petrology, 45, 855-881.

635 Deabate. S., Fourgeot, F., and Henn, F. (2000) X-ray diffraction and micro-Raman spectroscopy
636 analysis of new nickel hydroxide obtained by electrodialysis. Journal of Power Sources,
637 87, 125-136.
638 Desilvestro, J., Corrigan, D.A., and Weaver, M.J. (1986) Spectroelectrochemistry of thin nickel
639 hydroxide films on gold using surface-enhanced Raman spectroscopy. Journal of
640 Physical chemistry, 90, 6408-6411.
641 Dieterle, M., Mestl, G. (2002) Raman spectroscopy of molybdenum oxides Part II. Resonance
642 Raman spectroscopic characterization of the molybdenum oxides Mo_4O_{11} and MoO_2.
643 Physical Chemistry Chemical Physics, 4, 822-826.
644 Dixon, J.E., Stolper, E.M., and Holloway, J.R. (1995) An experimental study of water and
645 carbon dioxide solubilities in mid ocean ridge basaltic liquids .1. Calibration and
646 solubility models. Journal of Petrology, 36, 1607-1631.
647 Draper, D.S., and Green, T.H. (1997) P-T phase relations of silicic, alkaline, aluminous mantle-
648 xenolith glasses under anhydrous and C-O-H fluid-saturated conditions. Journal of
649 Petrology, 38, 1187-1224.
650 Dubessy, J., Moissette, A., Bakker, R.J., Frantz, J.D., and Zhang, Y.G. (1999) High-temperature
651 Raman spectroscopic study of H_2O-CO_2-CH_4 mixtures in synthetic fluid inclusions: First
652 insights on molecular interactions and analytical implications. European Journal of
653 Mineralogy, 11, 23-32.
654 Eck, R.V., Lippinco.Er, Dayhoff, M.O., and Pratt, Y.T. (1966) Thermodynamic equilibrium and
655 inorganic origin of organic compounds. Science, 153, 628-633.

656 Eggler, D.H., Mysen, B.O., Hoering, T.C., and Holloway, J.R. (1979) Solubility of carbon
657 monoxide in silicate melts at high pressure and its effect on silicate phase relations. Earth
658 and Planetary Science Letters, 43, 321-330.
659 Fegley, B., Zolotov, M.Y., and Lodders, K. (1997) The oxidation state of the lower atmosphere
660 and surface of Venus. Icarus, 125, 416-439.
661 Frantz, J.D., Dubessy, J., and Mysen, B. (1993) An optical cell for Raman spectroscopic studies
662 of supercritical fluids and its application to the study of water to 500^{o}C and 2000 bar.
663 Chemical Geology, 106, 9-26.
664 Frost, R.L., Reddy, B.J., Dickfos, M.J. (2008) Raman spectroscopy of hydroxy nickel carbonate
665 minerals nullaginite and zaratite. Journal of Raman Spectroscopy, 39, 1250-1256.
666 Helgeson, H.C. (1979) Mass transfer among minerals and hydrothermal solutions. In H.L.
667 Barnes, EdGeochemistry of hydrothermal ore deposits, p. 798. Wiley, New York.
668 Helgeson, H.C., Delany, J.M., Nesbitt, H.W., and Bird, D.K. (1978) Summary and critique of the
669 thermodynamic properties of rock-forming minerals. American Journal of Science, 278,
670 1-229.
671 Holloway, J.R., and Jakobsson, S. (1986) Volatile solubilities in magmas: Transport of volatiles
672 from mantles to planet surfaces. Journal of Geophysical Research-Solid Earth and
673 Planets, 91, D505-D508.
674 Holloway, J.R., and Reese, R.L. (1974) Generation of N_2-CO_2-H_2O fluids for use in
675 hydrothermal experimentation Part 1: Experimental method and equilibrium calculations
676 in the C-O-H-N system. American Mineralogist, 59, 587-597.

677 Holloway, J.R., Burnham, C.W., and Millhollen, G.L. (1968) Generation of H_2O-CO_2 mixtures
678 for use in hydrothermal experimentation. Journal of Geophysical Research, 73, 6598-
679 6600.
680 Holmes, R.D., Oneill, H.S.C., and Arculus, R.J. (1986) Standard Gibbs free energy of formation
681 for Cu_2O, NiO, CoO, and FexO: High resolution electrochemical measurements using
682 zirconia solid electrolytes from 900-1400K. Geochimica Et Cosmochimica Acta, 50,
683 2439-2452.
684 Jakobsson, S., and Holloway, J.R. (1986) Crystal-liquid experiments in the presence of a C-O-H
685 fluid buffered by graphite + iron + wustite: Experimental method and near-liquidus
686 relations in basanite. Journal of Volcanology and Geothermal Research, 29, 265-291.
687 Jakobsson, S., and Oskarsson, N. (1990) Experimental determination of fluid compositions in the
688 system C-O-H at high P and low f_{O2}. Geochimica Et Cosmochimica Acta, 54, 355-362.
689 Jambon, A. (1994) Earth degassing and large-scale geochemical cycling of volatile elements.
690 Reviews in Mineralogy: Volatiles in Magmas, 30, 479-517.
691 Johnson, J.W., Oelkers, E.H., and Helgeson, H.C. (1992) SUPCRT92 - A software package for
692 calculating the standard molal thermodynamic properties of minerals, gases, aqueous
693 species, and reactions from 1 bar to 5000 bars and 0^oC to 1000^oC. Computers &
694 Geosciences, 18, 899-947.
695 Kadik, A., Pineau, F., Litvin, Y., Jendrzejewski, N., Martinez, I., and Javoy, M. (2004)
696 Formation of carbon and hydrogen species in magmas at low oxygen fugacity. Journal of
697 Petrology, 45, 1297-1310.
698 Kakumoto, T., Saito, K., and Imamura, A. (1987) Unimolecular decomposition of oxalic acid.
699 Journal of Physical Chemistry, 91, 2366-2371.

Kawamoto, T., Ochiai, S., and Kagi, H. (2004) Changes in the structure of water deduced from the pressure dependence of the Raman OH frequency. Journal of Chemical Physics, 120, 5867-5870.

Kesson, S.E., and Holloway, J.R. (1974) Generation of N_2-CO_2-H_2O fluids for use in hydrothermal experimentation Part 2: Melting of albite in a multispecies fluid. American Mineralogist, 59, 598-603.

Lapidus, G., Yankwich, P.E., and Barton, D. (1964) Kinetics + stoichiometry of gas-phase decomposition of oxalic acid. Journal of Physical Chemistry, 68, 1863-1865.

Lin, F., and Bodnar, R.J. (2010) Synthetic fluid inclusions XVIII: Experimental determination of the PVTX properties of H_2O CH_4 to 500 ^oC, 3 kbar and X-CH4 <= 4 mol.%. Geochimica et Cosmochimica Acta, 74, 3260-3273.

Lin-vien, D., Colthup, N.B., Fateley, W.G., and Grasselli, J.G. (1991) The Handbook of Infrared and Raman Characteristic Frequencies of Organic Molecules. Academic Press, 497 pp.

Litvinovsky, B.A., Steele, I.M., and Wickham, S.M. (2000) Silicic magma formation in overthickened crust: Melting of charnockite and leucogranite at 15, 20, and 25 kbar. Journal of Petrology, 41, 717-737.

Lu, W.J., Chou, I-M., Burruss, R. C., and Song, Y.C. (2007) A unified equation for calculating methane vapor pressures in the CH_4-H_2O system with measured Raman shifts. Geochimica et Cosmochimica Acta, 71, 3969-3978.

Luque, F.J., Pasteris, J.D., Wopenka, B., Rodas, M., and Barrenechea, J.F. (1998) Natural fluid-deposited graphite: Mineralogical characteristics and mechanisms of formation. American Journal of Science, 298, 471-498.

McCubbin, F.M., Riner, M.A., Vander Kaaden, K.E., and Burkemper, L.K. (2012) Is Mercury a volatile-rich planet? Geophysical Research Letters, 39, 1-5.

McMillan, P.F., and Remmele, R.L. (1986) Hydroxyl sites in SiO_2 glass: A note on infrared and Raman spectra. American Mineralogist, 71, 772-778.

Morgan, G.B., Chou, I.M., and Pasteris, J.D. (1992) Speciation in experimental C-O-H fluids produced by the thermal dissociation of oxalic-acid dihydrate. Geochimica et Cosmochimica Acta, 56, 281-294.

Mysen, B. (2010) Structure of H_2O-saturated peralkaline aluminosilicate melt and coexisting aluminosilicate-saturated aqueous fluid determined *in-situ* to 800^{o}C and 800 MPa. Geochimica Et Cosmochimica Acta, 74, 4123-4139.

Mysen, B.O., and Yamashita, S. (2010) Speciation of reduced C-O-H volatiles in coexisting fluids and silicate melts determined in-situ to similar to 1.4 GPa and 800 degrees C. Geochimica et Cosmochimica Acta, 74, 4577-4588.

Mysen, B.O., Arculus, R.J., and Eggler, D.H. (1975) Solubility of carbon dioxide in melts of andesite, tholeite, and olivine nephelinite composition to 30 kbar pressure. Contributions to Mineralogy and Petrology, 53, 227-239.

Nieminen, J., Rasanen, M., and Murto, J. (1992) Matrix-isolation and ab initio studies of oxalic acid. Journal of Physical Chemistry, 96, 5303-5308.

Noyes, W.A., and Wobbe, D.E. (1926) The vapor pressure of anhydrous oxalic acid. Journal of the American Chemical Society, 48, 1882-1887.

O'Neill, H.S.C. (1986) Mo-MoO_2 (MOM) oxygen buffer and the free energy of formation of MoO_2. American Mineralogist, 71, 1007-1010.

-. (1987) Quartz-fayalite-iron and quartz-fayalite-magnetite equilibria and the free energy of formation of fayalite (Fe_2SiO_4) and magnetite (Fe_3O_4) American Mineralogist, 72, 67-75.

O'Neill, H.S., and Pownceby, M.I. (1993) Thermodynamic data from redox reactions at high temperatures Part 1: An experimental and theoretical assessment of the electrochemical method using stabalized zirconia electrolytes, with revised values for the Fe-FeO, Co-CoO, Ni-NiO, and Cu-Cu_2O oxygen buffers and new data for the W-WO_2 buffer. Contributions to Mineralogy and Petrology, 114, 296-314.

Peng, G.Y., Luhr, J.F., and McGee, J.J. (1997) Factors controlling sulfur concentrations in volcanic apatite. American Mineralogist, 82, 1210-1224.

Robie, R.A., Hemingway, D.S., and Fisher, R. (1978) Thermodynamic properties of minerals and related substances at 298.15 K and 1 bar (10^5 pascals) pressure and at higher temperatures. U. S. Geological Survey Bulletin, 1452, 456.

Rosenbaum, J.M., and Slagel, M.M. (1995) C-O-H speciation in piston-cylinder experiments. American Mineralogist, 80, 109-114.

Rosso, K.M., and Bodnar, R.J. (1995) Microthermometric and Raman spectroscopic detection limits of CO_2 in fluid inclusions and the Raman spectroscopic characterization of CO_2. Geochimica et Cosmochimica Acta, 59, 3961-3975.

Saxena, S.K., and Fei, Y. (1987) High pressure and high temperature fluid fugacities. Geochimica et Cosmochimica Acta, 51, 783-791.

Schmidt, C. (2009) Raman spectroscopic study of a H_2O + Na_2SO_4 solution at 21-600 ^{0}C and 0.1 MPa to 1.1 GPa: Relative differential ν_1-SO_4^{2-} Raman scattering cross sections and evidence of the liquid-liquid transition. Geochimica et Cosmochimica Acta, 73, 425-437.

766 Sharp, Z.D., McCubbin, F.M., and Shearer Jr, C.K. (2013) A hydrogen-based oxidation
767 mechanism relevant to planetary formation. Earth and Planetary Science Letters, 380, 88-
768 97.
769 Shock, E.L. (1995) Organic acids in hydrothermal solutions: Standard molal thermodynamic
770 properties of carboxylic acids and estimates of dissociation-constants at high
771 temperatures and pressures. American Journal of Science, 295, 496-580.
772 Shock, E.L., and Helgeson, H.C. (1988) Calculation of the thermodynamic and transport
773 properties of aqueous species at high pressures and temperatures: Correlation algorithms
774 for ionic species and equation of state predictions to 5 kbar and 1000°C. Geochimica et
775 Cosmochimica Acta, 52, 2009-2036.
776 -. (1990) Calculation of the thermodynamic and transport properties of aqueous species at high
777 pressures and temperatures: Standard partial molal properties of organic species.
778 Geochimica et Cosmochimica Acta, 54, 915-945.
779 Shock, E.L., Helgeson, H.C., and Sverjensky, D.A. (1989) Calculation of the thermodynamic
780 and transport properties of aqueous species at high pressures and temperatures: Standard
781 partial molal properties of inorganic neutral species. Geochimica et Cosmochimica Acta,
782 53, 2157-2183.
783 Shock, E.L., Sassani, D.C., Willis, M., and Sverjensky, D.A. (1997) Inorganic species in
784 geologic fluids: Correlations among standard molal thermodynamic properties of aqueous
785 ions and hydroxide complexes. Geochimica et Cosmochimica Acta, 61, 907-950.
786 Socrates, G. (2001) Infrared and Raman characteristic group frequencies: Tables and charts. John
787 Wiley & Sons, New York. 366 pp.

788 Steele, A., Fries, M.D., Amundsen, H.E.F., Mysen, B.O., Fogel, M.L., Schweizer, M., and
789 Boctor, N.Z. (2007) Comprehensive imaging and Raman spectroscopy of carbonate
790 globules from Martian meteorite ALH 84001 and a terrestrial analogue from Svalbard.
791 Meteoritics & Planetary Science, 42, 1549-1566.
792 Steele, A., McCubbin, F.M., Fries, M., Glamoclija, M., Kater, L., and Nekvasil, H. (2010)
793 Graphite in an Apollo 17 impact melt breccia. Science, 329, 51-51.
794 Steele, A., McCubbin, F.M., Fries, M., Kater, L., Boctor, N.Z., Fogel, M.L., Conrad, P.G.,
795 Glamoclija, M., Spencer, M., Morrow, A.L., Hammond, M.R., Zare, R.N., Vicenzi, E.,
796 Siljestrom, S., Bowden, R., Herd, C.D.K., Mysen, B.O., Shirey, S.B., Amundsen, H.E.F.,
797 Treiman, A.H., Bullock, E.S., and Jull, A.J.T. (2012a) A reduced organic carbon
798 component in martian basalts. Science, 337, 212-215.
799 Steele, A., McCubbin, F.M., Fries, M.D., Golden, D.C., Ming, D.W., and Benning, L.G. (2012b)
800 Graphite in the martian meteorite Allan Hills 84001. American Mineralogist, 97, 1256-
801 1259.
802 Stein, S.E. (1978) High temperature chemical equilibria of polycyclic aromatic hydrocarbons.
803 Journal of Physical Chemistry, 82, 566-571.
804 -. (1991) Thermal reactions and properties of polycyclic aromatic hydrocarbons. Accounts of
805 Chemical Research, 24, 350-356.
806 Stein, S.E., and Fahr, A. (1985) High temperature stabilities of hydrocarbons. Journal of Physical
807 Chemistry, 89, 3714-3725.
808 Sverjensky, D.A., Shock, E.L., and Helgeson, H.C. (1997) Prediction of the thermodynamic
809 properties of aqueous metal complexes to 1000^{o}C and 5 kbar. Geochimica et
810 Cosmochimica Acta, 61, 1359-1412.

Ulmer, P., and Luth, R.W. (1991) The graphite-C-O-H fluid equilibrium in P, T, f_{O2} space: An experimental determination to 30 kbar and 1600°C. Contributions to Mineralogy and Petrology, 106, 265-272.

Van Thiel, M., Becker, E.D., and Pimentel, G.C. (1957) Infrared studies of hydrogen bonding of water by the matrix isolation technique. Journal of Chemical Physics, 27, 486-490.

Velde, B. (1983) Infrared OH-stretching bands in potassic micas, talcs, and saponites: Influence of electronic configuration and site of charge compensation. American Mineralogist, 68, 1169-1173.

Wagner, W., and Pruss, A. (2002) The IAPWS formulation 1995 for the thermodynamic properties of ordinary water substance for general and scientific use. Journal of Physical and Chemical Reference Data, 31, 387-535.

Wobbe, D.E., and Noyes, W.A. (1926) Photochemical studies IV: The thermal decomposition of anhydrous oxalic acid and its relation to the photochemical decomposition. Journal of the American Chemical Society, 48, 2856-2868.

Wolery, T.J. (1983) EQ3NR: A computer program for geochemical aqueous speciation-solubility calculations, user's guide and documentation. Lawrence Livermore Laboratory, University of California.

-. (1984) EQ6: A computer program for reaction-path modeling of aqueous geochemical systems: User's guide and documentation. Lawrence Livermore National Laboratory, University of California.

Yamamoto, J., and Kagi, H. (2008) Application of densimetry using micro-Raman spectroscopy for CO(2) fluid inclusions: a probe for elastic strengths of mantle minerals. European Journal of Mineralogy, 20, 529-535.

834 Yamamoto, S., and Back, R.A. (1985) The gas-phase photochemistry of oxalic acid. Journal of
835 Physical Chemistry, 89, 622-625.
836 Zhang, C., and Duan, Z.H. (2009) A model for C-O-H fluid in the Earth's mantle. Geochimica et
837 Cosmochimica Acta, 73, 2089-2102.
838 -. (2010) GFluid: An Excel spreadsheet for investigating C-O-H fluid composition under high
839 temperatures and pressures. Computers & Geosciences, 36, 569-572.
840 Zhang, H., Ling, M.X., Liu, Y.L., Tu, X.L., Wang, F.Y., Li, C.Y., Liang, H.Y., Yang, X.Y.,
841 Arndt, N.T., and Sun, W.D. (2013) High Oxygen Fugacity and Slab Melting Linked to
842 Cu Mineralization: Evidence from Dexing Porphyry Copper Deposits, Southeastern
843 China. Journal of Geology, 121, 289-305.
844 Zolotov, M.Y., Sprague, A.L., Hauck, S.A., Nittler, L.R., Solomon, S.C., and Weider, S.Z.
845 (2013) The redox state, FeO content, and origin of sulfur-rich magmas on Mercury.
846 Journal of Geophysical Research-Planets, 118, 1-9.
847
848
849
850
851
852
853
854
855
856

857 **Figure captions**

858

859 Figure 1. The logf_{O2} values for the buffer curves FMQ, IW, GCO, MMO, and NiNiO are
860 illustrated following an isopleth that approximates our experimental run conditions to illustrate
861 how the slopes of the buffer curves change relative to one another as a function of the P-T path
862 in the HDAC experiments conducted in the present study. Data for the buffer curves come from
863 a number of sources (Holmes et al., 1986; O'Neill, 1987; O'Neill and Pownceby, 1993; O'Neill,
864 1986; Ulmer and Luth, 1991)

865

866 Figure 2. Photomicrographs of the Mo^0-bearing and unbuffered HDAC experiments at
867 various stages of heating/compression and cooling/decompression. All phases in each of the
868 photomicrographs has been identified. Scale bar in d applies to images a and d and scale bar in e
869 applies to images b, c, e, f. a) Mo-bearing experiment with 160 mM oxalic acid solution in the Ir
870 gasket along with some air bubbles b) Mo-bearing experiment during the cooling step showing
871 Mo that has transformed to MoO_2 c) Mo-bearing experiment during cooling just after vapor
872 exsolution. d) Unbuffered experiment with 160 mM oxalic acid solution loaded in the Ir gasket
873 e) Unbuffered experiment at 800°C and 1450 MPa, soon after graphitic carbon precipitation f)
874 Unbuffered experiment subsequent to cooling and decompression at 25°C after the vapor
875 exsolved at about 90°C.

876

877 Figure 3. Raman spectra of solid phases present within the HDAC experiments. a) MoO_2
878 at 25°C after cooling, b) $Ni(OH)_2$ at 25°C before heating, c) zaratite [$Ni_3(CO_3)(OH)_4$•$4(H_2O)$] at
879 300°C during heating. d) poorly crystalline zaratite at 600°C during heating e) poorly crystalline

880 zaratite at 700°C during cooling f) poorly crystalline zaratite at 100°C during cooling. Phase
881 identifications were verified based on several literature references (Dieterle and Mestl, 2002;
882 Deabate et al., 2000; Desilvestro et al., 1986; Frost et al., 2008).
883
884 Figure 4. Raman spectra of the fluid in the Mo-bearing HDAC experiment. a) Raman
885 spectra collected at 100°C intervals during the entire duration of the Mo-bearing HDAC
886 experiment. Each spectrum is labeled with the temperature conditions at which the spectrum was
887 collected, and each of the Raman modes have been identified. The dotted regions represent
888 certain regions that were blown up in parts b and c to illustrate specific Raman modes b) Raman
889 spectral features from the Mo-bearing experiments focusing on the stretching region that is
890 typically associated with C-H_n vibration modes. The dotted box labeled b. in Figure 4a is the
891 region displayed for this portion of the figure. c) Raman spectral features from the Mo-bearing
892 experiments focusing on the stretching region that is typically associated with H_2 vibration
893 modes. The dotted box labeled c. in Figure 4a is the region displayed for this portion of the
894 figure.
895
896 Figure 5. Raman spectra of the vapor phases in the Mo-bearing HDAC experiment. a)
897 Raman spectra collected at 50°C intervals subsequent to vapor exsolution that occurred during
898 cooling and decompression of the Mo-bearing HDAC experiment. Each spectrum is labeled with
899 the temperature conditions at which the spectrum was collected, and each of the Raman modes
900 have been identified.
901

Figure 6. Photomicrographs of the Ni^0- and NiO-bearing HDAC experiment at various stages of heating/compression and cooling/decompression. All phases in each of the photomicrographs has been identified a) Ni^0 + NiO-bearing experiment before heating with 160 mM oxalic acid solution in the Ir gasket showing substantial formation of $Ni(OH)_2$ b) Experiment during the heating step showing substantial formation of zaratite $[Ni_3(CO_3)(OH)_4 \bullet 4(H_2O)]$ c) Experiment during the heating step showing partial breakdown of zaratite to Ni^0 metal. d) Experiment during cooling and decompression, at 35°C subsequent to vapor exsolution at 50°C. Ni^0 and zaratite remain.

Figure 7. Raman spectra of the exsolved vapor phases in the Ni^0 + NiO HDAC experiment. a) Raman spectra collected at 35°C, spectrum centered at 1300 cm^{-1}. Each of the Raman modes are identified. b) Raman spectra collected at 25°C. Raman scan centered at 2900 cm^{-1} illustrating the absence of detectable C-H species in the exsolved vapor phase

Figure 8. Raman spectra of the fluid in the unbuffered HDAC experiment. a) Raman spectra collected at 100°C intervals during the entire duration of the unbuffered HDAC experiment. Each spectrum is labeled with the temperature conditions at which the spectrum was collected, and each of the Raman modes have been identified. The dotted regions represent certain regions that were blown up in parts b and c to illustrate specific Raman modes b) Raman spectral features from the unbuffered experiment focusing on the stretching region that is typically associated with C bonds in graphite. The dotted box labeled b. in Figure 8a is the region displayed for this portion of the figure. c) Raman spectral features from the unbuffered experiment focusing on the stretching region that is typically associated with $C\text{-}H_n$ vibration

925 modes. The dotted box labeled c. in Figure 8a is the region displayed for this portion of the
926 figure.
927
928 Figure 9. Raman spectra of the vapor phases in the unbuffered HDAC experiment. a)
929 Raman spectra collected at <100°C subsequent to vapor exsolution that occurred during cooling
930 and decompression of the unbuffered HDAC experiment. Each of the Raman modes have been
931 identified. The dotted regions represent certain regions that were blown up in parts b and c to
932 illustrate specific Raman modes b) Raman spectral features from the unbuffered experiment
933 focusing on the stretching region that is typically associated with CO_2 vibration modes. The
934 dotted box labeled b. in Figure 9a is the region displayed for this portion of the figure. c) Raman
935 spectral features from the unbuffered experiment focusing on the stretching region that is
936 typically associated with C-H_n and specifically CH_4 vibration modes. The dotted box labeled c.
937 in Figure 9a is the region displayed for this portion of the figure.

1

Table 1. Experimental run data.

160 mM $C_2H_2O_4$ (fluid density[a] = 0.997 g/cm^3)			160 mM $C_2H_2O_4$ + Mo^0 wire (fluid density[a] = 0.905 g/cm^3)			160 mM $C_2H_2O_4$ + Ni^0 + NiO (fluid density[a] = 0.997 g/cm^3)		
Temp. (°C)[b]	Press. (MPa)	Phase (assemblage)	Temp. (°C)[b]	Press. (MPa)	Phase (assemblage)	Temp. (°C)[b]	Press. (MPa)	Phase (assemblage)
25	-	Fluid	25	-	Fluid + Vapor + Mo^0	25	-	Fluid + Ni^0 + NiO + $Ni(OH)_2$
100	90	Fluid	100	<50	Fluid + Vapor + Mo^0	100	90	Fluid + Ni^0 + $Ni(OH)_2$ + $Ni_3(CO_3)(OH)_4$•4(H_2O)
200	290	Fluid	200	65	Fluid + Mo^0	200	290	Fluid + Ni^0 + $Ni(OH)_2$ + $Ni_3(CO_3)(OH)_4$•4(H_2O)
300	510	Fluid	300	240	Fluid + Mo^0	300	510	Fluid + Ni^0 + $Ni_3(CO_3)(OH)_4$•4(H_2O)
400	730	Fluid	400	420	Fluid + Mo^0	400	730	Fluid + Ni^0 + $Ni_3(CO_3)(OH)_4$•4(H_2O)
500	940	Fluid	500	600	Fluid + Mo^0 + MoO_2	500	940	Fluid + Ni^0 + $Ni_3(CO_3)(OH)_4$•4(H_2O)
600	1150	Fluid	600	770	Fluid + Mo^0 + MoO_2	600	1150	Fluid + Ni^0 + $Ni_3(CO_3)(OH)_4$•4(H_2O)
700	1340	Fluid	700	930	Fluid + Mo^0 + MoO_2	700	1340	Fluid + Ni^0 + $Ni_3(CO_3)(OH)_4$•4(H_2O)
800	1450[d]	Fluid + GC[c]	800	970[d]	Fluid + Mo^0 + MoO_2	800	1480[d]	Fluid + Ni^0 + $Ni_3(CO_3)(OH)_4$•4(H_2O)
700	1190	Fluid + GC[c]	700	700	Fluid + Mo^0 + MoO_2	700	1290	Fluid + Ni^0 + $Ni_3(CO_3)(OH)_4$•4(H_2O)
600	1000	Fluid + GC[c]	600	560	Fluid + Mo^0 + MoO_2	600	1100	Fluid + Ni^0 + $Ni_3(CO_3)(OH)_4$•4(H_2O)
500	810	Fluid + GC[c]	500	410	Fluid + Mo^0 + MoO_2	500	900	Fluid + Ni^0 + $Ni_3(CO_3)(OH)_4$•4(H_2O)
400	610	Fluid + GC[c]	400	270	Fluid + Mo^0 + MoO_2	400	700	Fluid + Ni^0 + $Ni_3(CO_3)(OH)_4$•4(H_2O)
300	400	Fluid + GC[c]	300	110	Fluid + Mo^0 + MoO_2	300	480	Fluid + Ni^0 + $Ni_3(CO_3)(OH)_4$•4(H_2O)
200	200	Fluid + GC[c]	200	<65	Fluid + Vapor + Mo^0 + MoO_2	200	260	Fluid + Ni^0 + $Ni_3(CO_3)(OH)_4$•4(H_2O)
100	15	Fluid + GC[c]	100	<10	Fluid + Vapor + Mo^0 + MoO_2	100	70	Fluid + Ni^0 + $Ni_3(CO_3)(OH)_4$•4(H_2O)
25	-	Fluid + GC[c] + Vapor	25	-	Fluid + Vapor + Mo^0 + MoO_2	25	-	Fluid + Ni^0 + Vapor + $Ni_3(CO_3)(OH)_4$•4(H_2O)

Notes: [a] Fluid density calculated based on liquid-vapor homogenization during heating using the PVT data for pure H_2O from Wagner and Pruss (2002). Liquid-vapor homogenization temperatures during heating were 25^{0}C, 162^{0}C, and 25^{0}C for the unbuffered, Mo-bearing, and Ni-NiO bearing experiments respectively. During cooling, the liquid-vapor homogenization temperatures were 90^{0}C (0.965 g/cm^3), 225^{0}C (0.834 g/cm^3), and 50^{0}C (0.988 g/cm^3) for the unbuffered, Mo-bearing, and Ni-NiO bearing experiments respectively.

[b] Temperatures for the experiments report the ramping up to 800°C and then ramping back down from 800°C.

[c] GC is an abbreviation for graphitic double-bonded (C=C) solid carbon phase.

[d] Pressure at 800 °C was computed based on the midpoint between the pressure computed using the density of the liquid determined during heating and the density of the liquid determined during cooling.

Table 2. Raman Peak data for fluid species in 160 mM $C_2H_2O_4$ + Mo^0 wire

CH_n-species				H_2-species			
Temp. (°C)	Peak center (cm^{-1})	Peak height[a]	FWHM	Temp. (°C)	Peak center (cm^{-1})	Peak height[a]	FWHM
100	*	*	*	100	*	*	*
200	*	*	*	200	*	*	*
300	*	*	*	300	*	*	*
400	*	*	*	400	*	*	*
500	2905.5	150.8	56.5	500	*	*	*
600	2920.1	478.6	30.4	600	*	*	*
700	2920.7	367.4	33.9	700	*	*	*
800	2910.3	333.6	33.5	800	*	*	*
700	2906.9	680.7	27.2	700	4132.9	219.6	21.7
600	2906.7	728.5	24.7	600	4128.9	245.0	20.6
500	2905.3	846.1	22.3	500	4129.7	277.5	17.8
400	2902.7	1004.9	18.6	400	4127.1	313.1	17.9
300	2901.3	1237.2	15.9	300	4126.9	381.1	17.5
200	2901.9	326.0	19.6	200	4125.5	119.4	23.0
100	2900.5	83.6	22.0	100	*	*	*

Notes: * Represents absence of a peak at this temperature.

[a] Peak heights were normalized based on the intensity of the primary second order diamond peak at ~2420-2450 cm^{-1} from each spectrum.

13

Table 3. Thermodynamic calculations for experimental HDAC system at 450°C and 500 MPa

Starting parameters	160 mM $C_2H_2O_4$		160 mM $C_2H_2O_4$ + Mo^0 wire[a]		160 mM $C_2H_2O_4$ + Ni^0 + NiO	
Run conditions	T = 450°C	P = 500 MPa	T = 450°C	P = 500 MPa	T = 450°C	P = 500 MPa
Computed conditions	pH = 3.8	$\log f_{O2}$ = -25.5	pH = 4.7	$\log f_{O2}$ = -32	pH = 4.3	$\log f_{O2}$ = -24.7
Aqueous Fluid Species	*Computed Concentration* [b]		*Computed Concentration* [c]		*Computed Concentration*	
CO_2	284 mM		Trace		320 mM	
CO	0.11 mM		Trace		Trace	
H_2	13 mM		< 6 M[d]		5.0 mM	
CH_4	37 mM		592 mM		1.0 mM	
Acetic acids and acid anions	Trace		Trace		Trace	
Mo-species	None		4.34×10^{-11} M[e]		None	
Graphite	Undersaturated (-4 kcal/mol)		Undersaturated (-24 kcal/mol)		Undersaturated (-7 kcal.mol)	

Notes: [a] Calculations included the reaction of 1.0 kg water with 20 moles Mo^0.

[b] Millimolar (mM) concentrations include the water derived from decomposition of oxalic acid to CO_2 and CH_4 (see text).

[c] Concentrations reflect the water consumed by the oxidation of 13.0 moles of the initial 20.0 moles of Mo to MoO_2.

[d] The maximum dissolved H_2(aq) when the partial pressure of H_2(g) is equal to the total pressure at 500 MPa.

[e] Final state of saturation in equilibrium with Mo^0 and MoO_2 solid phases.

14
15
16
17
18
19
20
21
22
23
24
25
26
27
28
29
30

Table 4. Raman Peak data for fluid species and solid phases in unbuffered 160 mM $C_2H_2O_4$

CH_n-species				Graphitic carbon phase			
Temp. (°C)	Peak center (cm^{-1})	Peak height[a]	FWHM	Temp. (°C)	Peak center (cm^{-1})	Peak height[a]	FWHM
100	*	*	*	100	*	*	*
200	*	*	*	200	*	*	*
300	*	*	*	300	*	*	*
400	2907.1	45.5	*	400	*	*	*
500	2910.7	27.6	27.7	500	*	*	*
600	2921.3	37.5	24.8	600	*	*	*
700	2935.1	24.2	29.2	700	*	*	*
800	*	*	*	800	1578.0	97.5	52.6
700	*	*	*	700	1574.5	109.6	46.9
600	2921.7	37.0	*	600	1578.3	119.3	49.7
500	2924.7	52.6	18.64	500	1582.7	135.5	48.6
400	2914.3	63.51	*	400	1584.1	147.4	45.9
300	*	*	*	300	1583.3	161.3	48.0
200	*	*	*	200	1585.3	192.5	49.3
100	*	*	*	100	1583.9	209.7	45.6

Notes: * Represents no data from this temperature.

[a] Peak heights were normalized based on the intensity of the primary second order diamond peak at ~2420-2450 cm^{-1} from each spectrum.

31

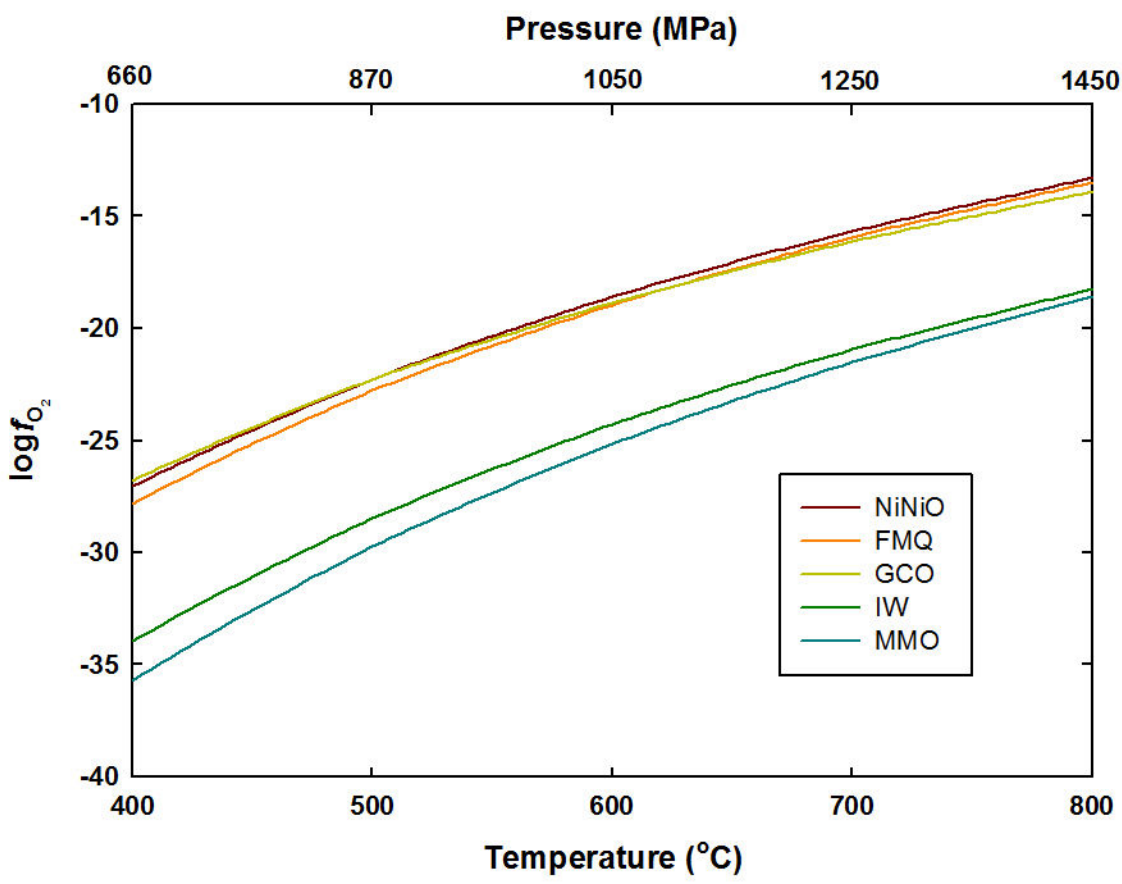
Pressure (MPa)
660
870
1050
1250
1450
-10
-15
-20
-25
-30
-35
-40
logf_{O_2}
400
500
600
700
800
Temperature (°C)
NiNiO
FMQ
GCO
IW
MMO

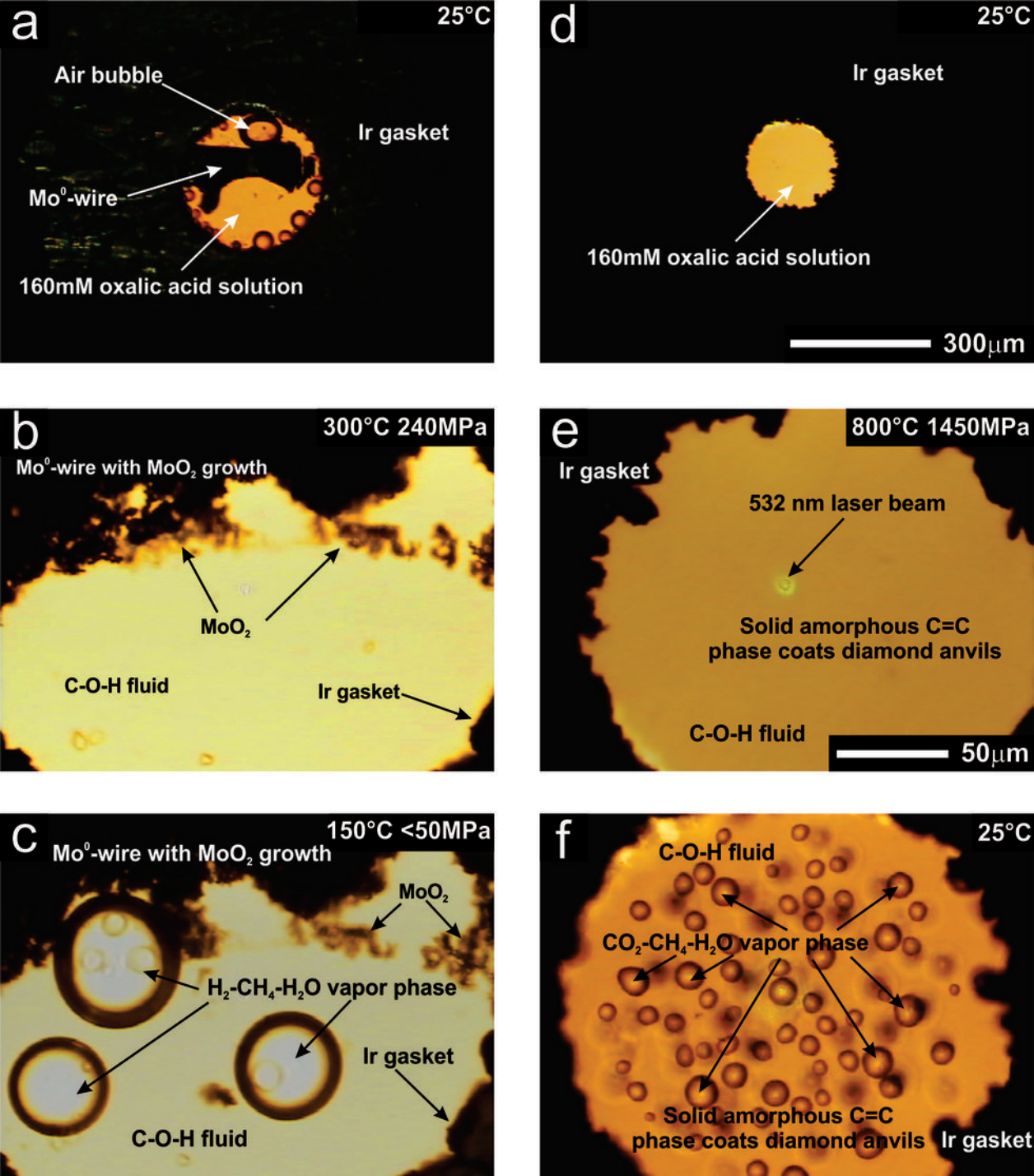
a
25°C
Air bubble
Ir gasket
Mo⁰-wire
160mM oxalic acid solution
d
25°C
Ir gasket
160mM oxalic acid solution
300μm
b
300°C 240MPa
Mo⁰-wire with MoO₂ growth
MoO₂
C-O-H fluid
Ir gasket
e
800°C 1450MPa
Ir gasket
532 nm laser beam
Solid amorphous C=C
phase coats diamond anvils
C-O-H fluid
50μm
c
150°C <50MPa
Mo⁰-wire with MoO₂ growth
MoO₂
H₂-CH₄-H₂O vapor phase
Ir gasket
C-O-H fluid
f
25°C
C-O-H fluid
CO₂-CH₄-H₂O vapor phase
Solid amorphous C=C
phase coats diamond anvils
Ir gasket

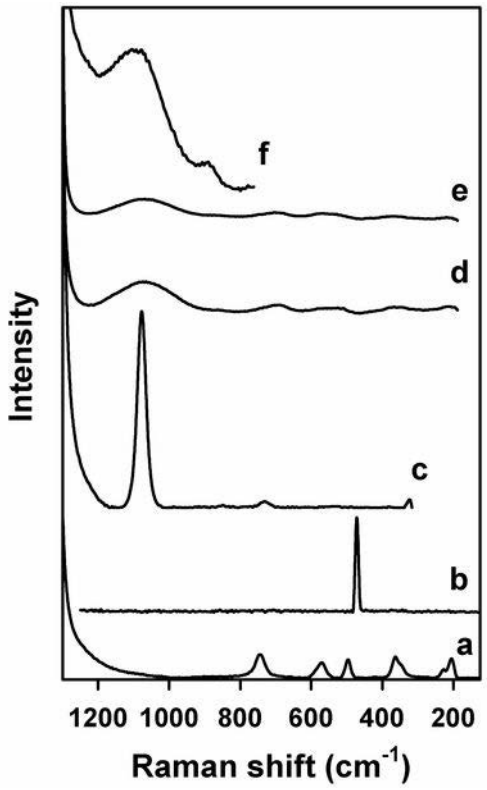
f
e
d
c
b
a
Intensity
1200 1000 800 600 400 200
Raman shift (cm-1)

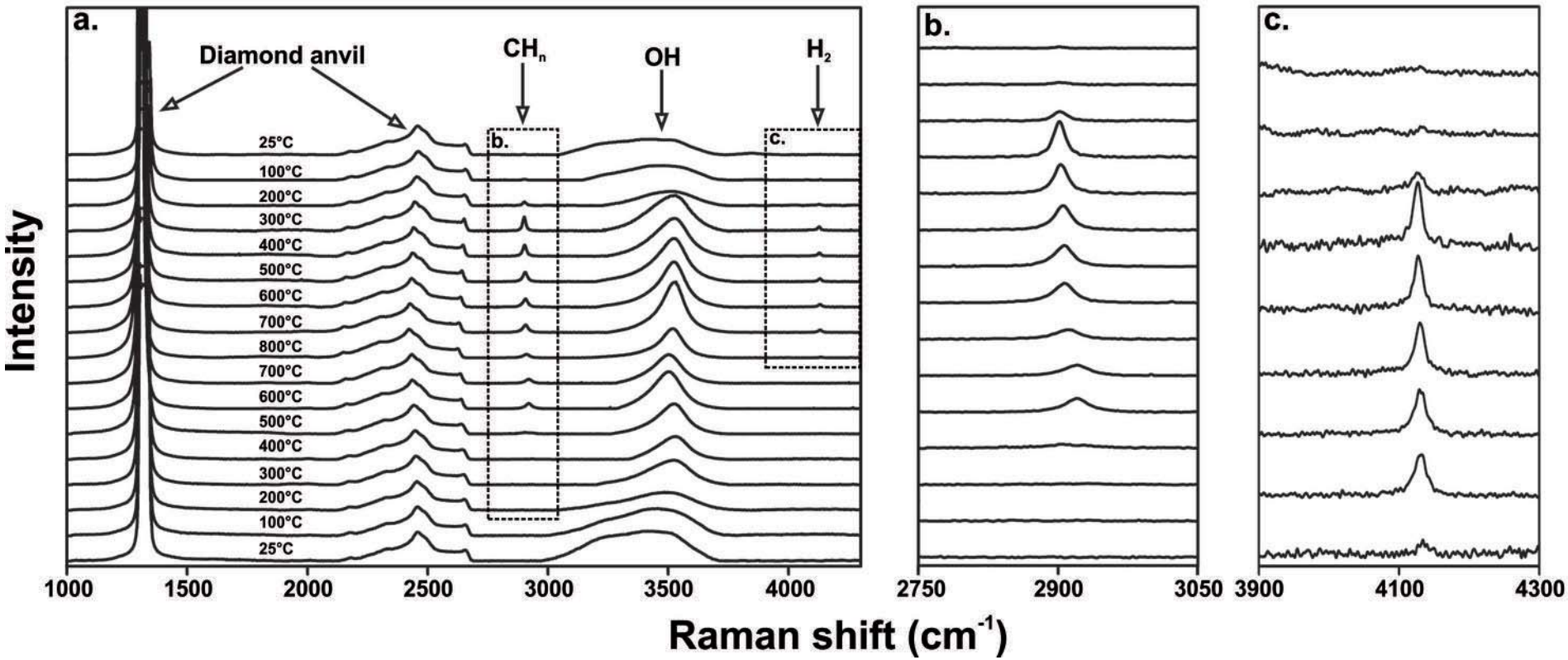
a.
Diamond anvil
CH$_n$
OH
H$_2$
b.
c.
25°C
100°C
200°C
300°C
400°C
500°C
600°C
700°C
800°C
700°C
600°C
500°C
400°C
300°C
200°C
100°C
25°C
Intensity
1000
1500
2000
2500
3000
3500
4000
2750
2900
3050
3900
4100
4300
Raman shift (cm^{-1})

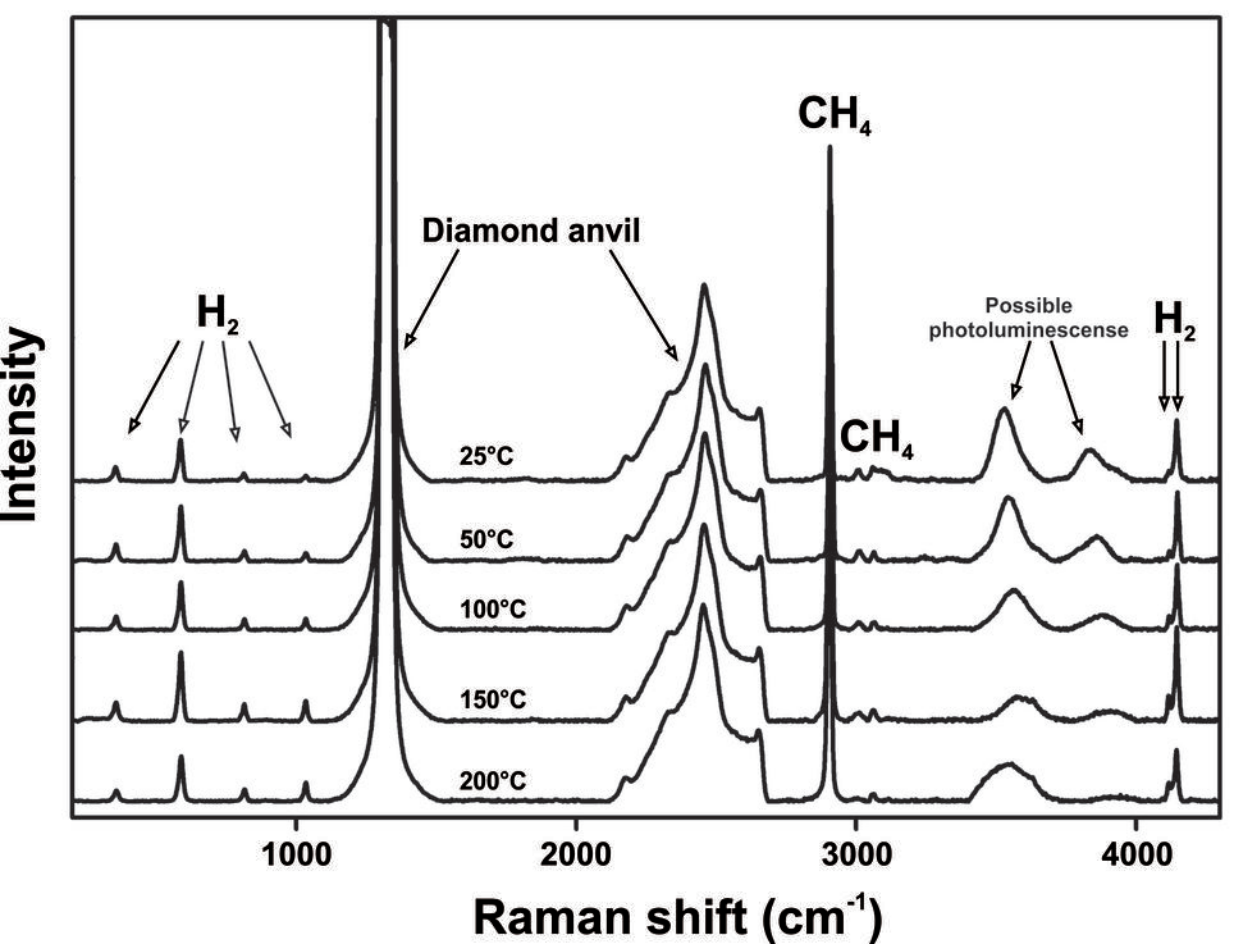
Intensity
Raman shift (cm-1)
H2
Diamond anvil
CH4
CH4
Possible photoluminescense
H2
25°C
50°C
100°C
150°C
200°C
1000
2000
3000
4000

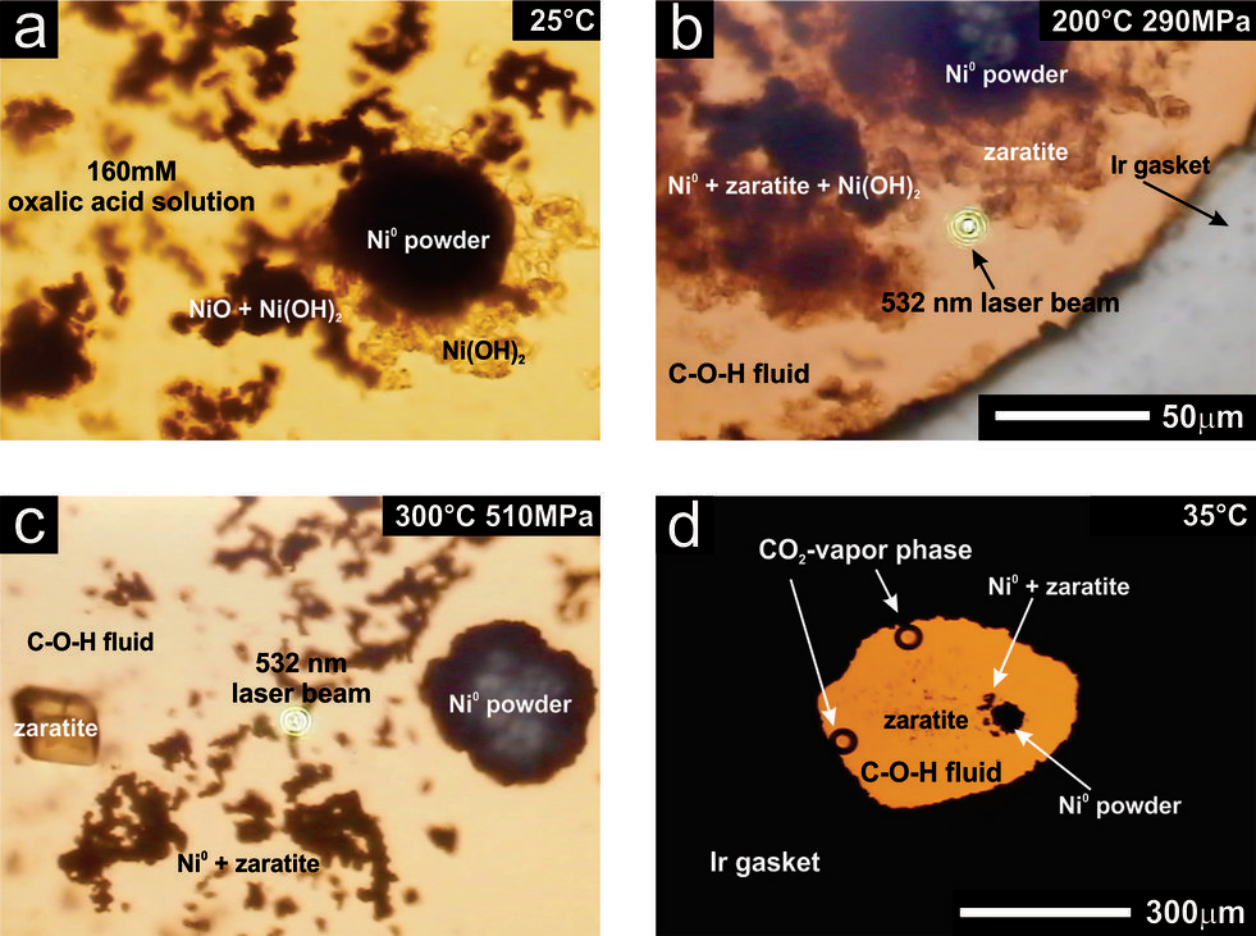
a
25°C
160mM
oxalic acid solution
Ni⁰ powder
NiO + Ni(OH)₂
Ni(OH)₂
b
200°C 290MPa
Ni⁰ powder
zaratite
Ir gasket
Ni⁰ + zaratite + Ni(OH)₂
532 nm laser beam
C-O-H fluid
50μm
c
300°C 510MPa
C-O-H fluid
532 nm
laser beam
Ni⁰ powder
zaratite
Ni⁰ + zaratite
d
35°C
CO₂-vapor phase
Ni⁰ + zaratite
zaratite
C-O-H fluid
Ni⁰ powder
Ir gasket
300μm

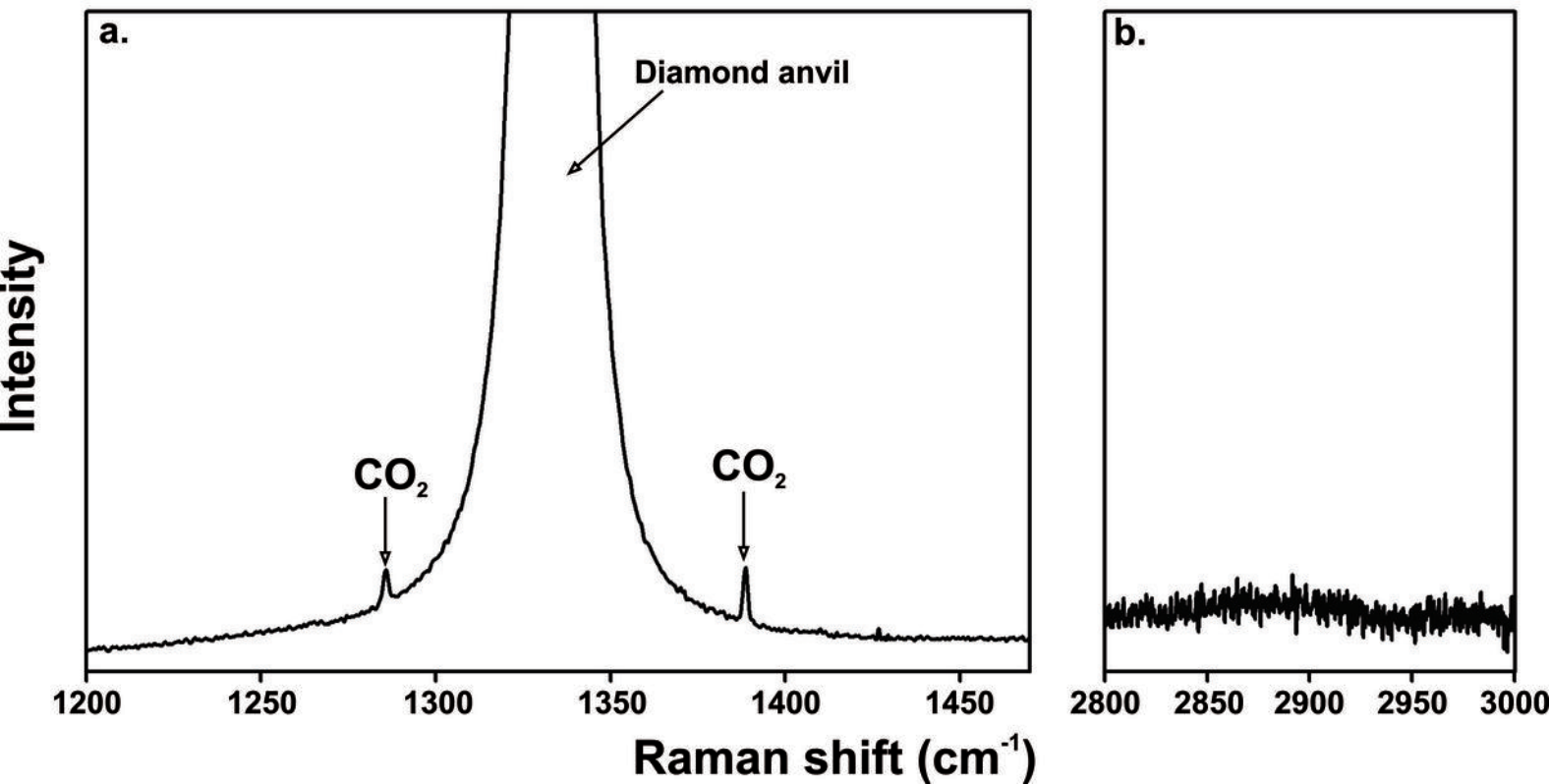
a.
b.
Diamond anvil
CO2
CO2
Intensity
1200
1250
1300
1350
1400
1450
2800
2850
2900
2950
3000
Raman shift (cm-1)

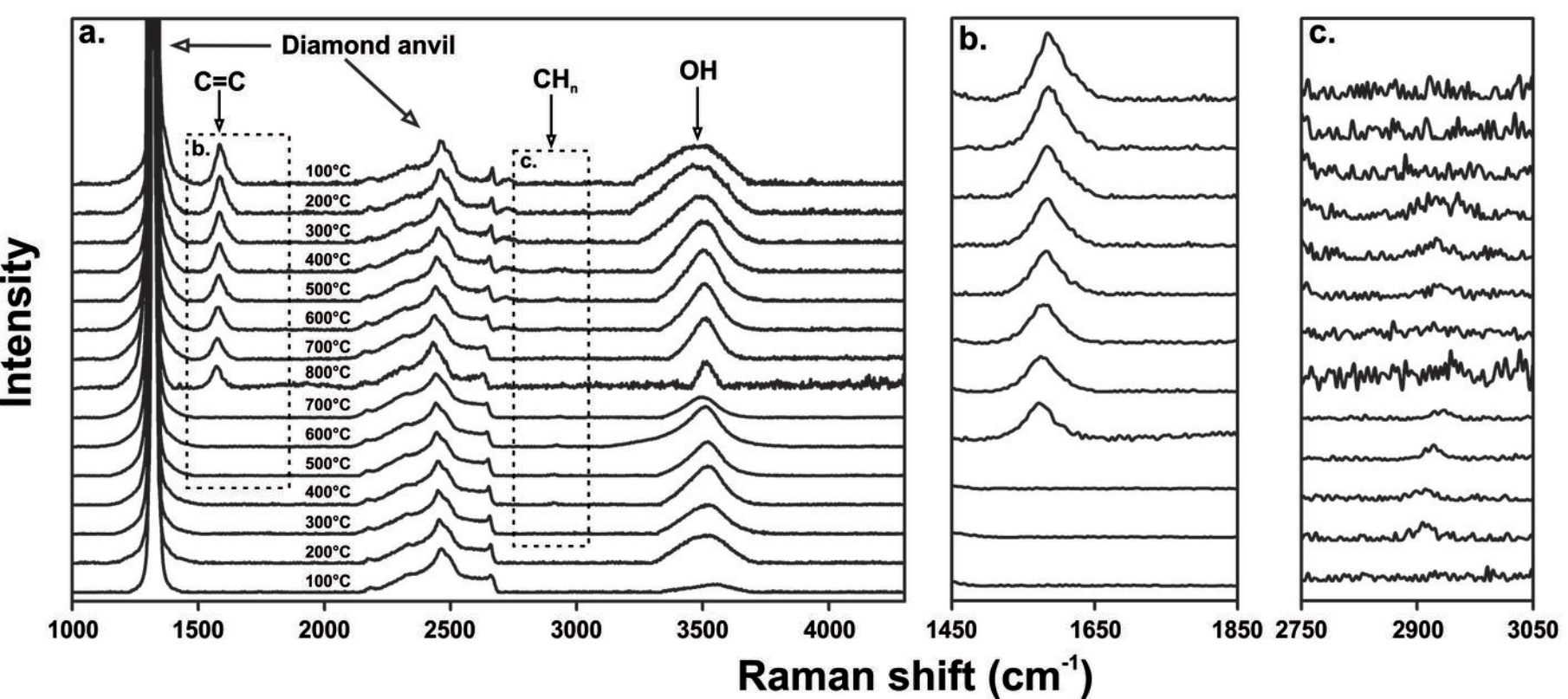
a.
Diamond anvil
C=C
CH$_n$
OH
b.
c.
100°C
200°C
300°C
400°C
500°C
600°C
700°C
800°C
700°C
600°C
500°C
400°C
300°C
200°C
100°C
Intensity
1000
1500
2000
2500
3000
3500
4000
b.
1450
1650
1850
c.
2750
2900
3050
Raman shift (cm^{-1})

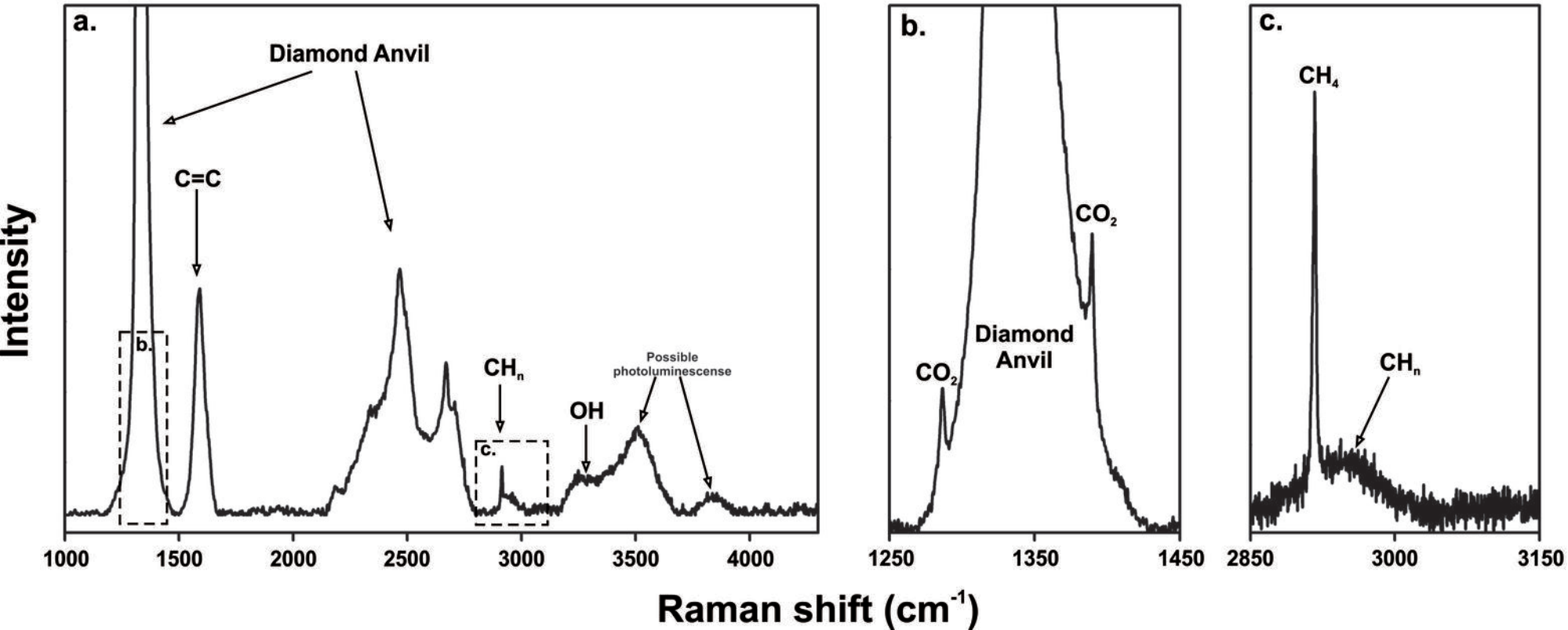
a.
Diamond Anvil
C=C
b.
CH$_n$
c.
OH
Possible
photoluminescense
1000
1500
2000
2500
3000
3500
4000
b.
CO$_2$
Diamond
Anvil
CO$_2$
1250
1350
1450
c.
CH$_4$
CH$_n$
2850
3000
3150
Intensity
Raman shift (cm^{-1})